Fermilab Library
0 1160 0003998 6

E594

NEUTRAL CURRENT AND CHARGED CURRENT STRUCTURE FUNCTIONS OF THE NUCLEON

by

Gong Ping Yeh

B. S. Massachusetts Institute of Technology

M. S. California Institute of Technology

SUBMITTED IN PARTIAL FULFILLMENT
OF THE REQUIREMENTS FOR THE
DEGREE OF DOCTOR OF PHILOSOPHY

at the

MASSACHUSETTS INSTITUTE OF TECHNOLOGY

Signature of Author . . . . . .
Physics Department
September 6, 1984

Certified by . . . . . .
Thesis Supervisor

Accepted by . . . . . .
Chairman, Physics Graduate
Committee

Abstract

An experimental determination of the neutral current structure functions of the nucleon is made from the ratio of the neutral current x distribution to the charged current x distribution. Deep Inelastic Neutrino–Nucleon scattering data have been taken using a massive fine-grained neutrino detector. The data are compared with the quark-parton model and the standard theory of Electromagnetic and Weak Interactions.

Acknowledgment

The success of this experiment is possible only with the great contribution of every member of the E594 Collaboration, and the enduring support of each member's family and friends. The members of the Collaboration are :

D. Bogert, R. Burnstein, R. Fisk, S. Fuess, J. Morfin,
M. Peters, L. Stutte, J. K. Walker

Fermi National Accelerator Laboratory

J. Bofill, W. Busza, T. Eldridge, J. I. Friedman, M. C. Goodman,
H.W.Kendall, V. Kistiakowsky, Tom Lyons, R. Magahiz, T. Mattison,
A. Mukherjee, L. S. Osborne, R. Pitt, L. Rosenson, A. Sandacz,
M. Tartaglia, F. E. Taylor, R. Verdier, J. S. Whitaker, G. P. Yeh

Massachusetts Institute of Technology

M. Abolins, R. Brock, A. Cohen, J. Ernwein,
D. Owen, J. Slate, H. Weerts

Michigan State University

In particular, I would like to thank Frank Taylor, my advisor during my stay at Fermilab. His tremendous dedication to physics has been a great inspiration.

My deepest gratitude goes to my advisor Jerry Friedman. His intuition and insight in physics are greatly admired; they have been crucial in

FERMILAB
LIBRARY

this analysis. Without his guidance, encouragement and strong support, this thesis would not have been possible.

Thanks also go to the Neutrino Department, the Film Analysis Facility, the Computing Department, the Users Office, and the entire Fermilab staff.

Contents

Introduction 8

I. Physics Motivation 13

I.1 Phenomenology of Deep Inelastic Scattering 13

I.2 Standard Theory of Electromagnetic, Weak and Strong Interactions 19

I.3 Predictions for Deep Inelastic Neutrino Scattering 22
I.3.1 Charged Current 22
I.3.2 Neutral Current 25

II. The Neutrino Beam 28

II.1 Principles of the Narrow Band Beam 28

II.2 Fermilab Narrow Band Beam 30

II.3 Beam Monitors for Total Secondary flux 32

II.4 Cerenkov Counter Pressure Curve 33
Average Momentum 33
Particle Fractions 34

II.5 Flux Calculation from Monte Carlo 34

III. The Lab C Detector 37

III.1 the Calorimeter 39

III.2 the Muon Spectrometer 42

III.3 Calibration and Resolutions 44

III.4 Trigger 56

IV. Event Reconstruction 59

IV.1 Event Selection 59

IV.1.1 Fiducial Volume 60

IV.1.2 Kinematic Cuts 61

IV.2 Monte Carlo Simulation 63

IV.3 CC or NC Classification 65

IV.4 Kinematic Reconstruction 71

V. Charged Current Analysis 72

Comparisons with Monte Carlo 72

VI. Neutral Current Analysis, with comparison to Charged Current 77

VI.1 The Distributions 77

VI.2 The Ratio Tests 80

VI.3 $\sin^2 \theta_w$ 90

VI.4 Background and Corrections : 93

VI.4.1 CC and NC misidentification 93

VI.4.2 Muon Bremsstrahlung 94

VI.4.3 Radiative Correction 94

VI.4.4 Resolutions 95

VI.4.5 K band contamination 96

VI.4.6 Wide band Background 97

VI.4.7 Neutron Excess 98

VI.4.8 Fermi Motion 99

VI.4.9 $s(x) - c(x)$ 99

VI.4.10 EMC Effect 100

VII. Conclusions 102

References 103

Introduction

In recent years, great progress has been made towards the understanding of the basic building blocks and the fundamental forces of nature. The purpose of the experiment described herein has been to contribute to this understanding.

By the 1960's, it had become well known that there are four fundamental forces of nature. The electron and the muon interact predominantly via the electromagnetic force. The neutrino interacts via the weak force, while the nucleon and all other hadrons interact primarily through the strong force. We feel the presence of the the gravitational force in our daily experiences. These four forces are vastly different in range and strength.

A major step towards the goal of unveiling the most basic building blocks of nature was made in 1968, when the MIT–SLAC Deep Inelastic Electron Scattering experiment(1) discovered that the nucleon was made of point–like constituents. Analogous to the Rutherford Scattering experiment, cross-sections that were expected to fall quickly with increasing momentum transfer showed only slight decrease. The results of the experiment were interpreted(2), in the context of the parton model(3), as indicating that the nucleon was composed of valence quarks, a sea of

quarks and antiquarks, and neutral particles called gluons–the particles that hold the nucleon together.

Neutrino scattering experiments[4,5,6] in the 1970's provided further support for the quark–parton model of hadrons. From the comparisons between experiments using a charged lepton or the the neutrino as a probe of the nucleon, we have learned that the electromagnetic current and the weak charged current see the same constituents of the nucleon. The Deep Inelastic Lepton–Nucleon Scattering experiments[1,4,5,6,7] have studied the distribution and interaction of quarks inside the nucleon, and have played a major role in the development of Quantum Chromodynamics (QCD)[8], the theory of strong interactions.

A major development in theoretical physics in recent years was the gauge theory[9] of electromagnetic and weak interactions. It represented a significant step towards the unified theory of the four fundamental forces in nature. The theory predicted the existence of the weak neutral current, its couplings in terms of a single free parameter, $\sin^2 \theta_W$, the existence of heavy gauge bosons as mediators of the weak force, and the couplings of these bosons to other particles.

The weak neutral current interaction was first observed experimentally in 1973,[10] and has subsequently been studied in a wide variety

of experiments, such as : 1. purely leptonic neutrino–electron scattering,[11] 2. neutral current and electromagnetic current interference in deep inelastic electron and muon scattering off the nucleon,[12] and in electron–positron interactions,[13] 3. semi–leptonic neutrino–nucleon scattering,[14] and 4. proton–antiproton collisions.[15,16] These data are consistent with the predictions from the "standard theory" of electromagnetic and weak interactions; however, data with more precision should be obtained from each of these processes to provide stringent tests of the theory.

The standard theory, together with the quark–parton model, made definite predictions for neutral current deep inelastic neutrino–nucleon scattering. Assuming that the neutral current sees the same constituents in the nucleon as does the charged current, recent [14] experiments have determined the value of $\sin^2\theta_W$ from neutral current total cross section and the y (fractional energy loss of the incident neutrino) distribution.[17]

The main goal of this experiment is to determine the neutral current structure functions to verify that the neutral current and the charged current see the same constituents in the nucleon. The goal presents a considerable challenge, and when the experiment was initiated, little

data existed on neutral current structure functions. [18,19,20]

In a neutral current neutrino interaction, the outgoing lepton is a neutrino which is not observed. Thus, the kinematics of the interaction must be reconstructed using the energy and angle of the hadron shower. This requires a target–detector of sufficient mass to achieve a statistically significant number of events, and yet has a fine enough granularity to measure the energy and angle of the hadron shower.

Such a detector has been constructed in Lab C at Fermilab by a collaboration consisting of Fermi National Accelerator Laboratory, Massachusetts Institute of Technology, Michigan State University, and Northern Illinois University. Data taken with this neutrino detector have been analyzed to obtain results on the determination of the neutral current structure functions, and of the value of $\sin^2 \theta_w$, which are presented in this thesis.

The organization of this thesis is as follows. In Chapter I, the kinematics of Deep Inelastic Scattering is defined, followed by a brief description of the standard theory of electromagnetic and weak interactions, and the predictions for neutrino interactions. The neutrino beam used in this experiment is described in Chapter II. Chapter III describes the neutrino detector in Lab C. In Chapter IV, the event reconstruction

and selection is described. The result of the analysis for the charged current events is summarized in Chapter V, and the result of the analysis of the neutral current events is presented in Chapter VI. Conclusions are presented in Chapter VII.

I. Physics Motivation

I.1 Phenomenology of Deep Inelastic Scattering

The basic cross section for an electron of incident energy E scattering off a spin $\frac{1}{2}$ point–like particle of mass m and charge z is

$$\frac{d\sigma}{dy} = \frac{4\pi\alpha^2 s}{(Q^2)^2}[1 - y + \frac{y^2}{2}]z^2 \qquad (I.1)$$

where $\alpha = e^2/4\pi$. The Feynman diagram for this process, in the one photon exchange approximation, is shown in Fig. I.1.a. In Eq. $I.1$, we have neglected a term $-my/2E$ (which is small when $E \gg m$) inside the square bracket. It is customary to define E' to be the energy of the outgoing electron, and $\nu = E - E'$ as the energy transfered to the target particle, and q as the four–momentum transfered. Two Lorentz invariant variables present in Eq. $I.1$ are (neglecting terms of order m^2)

$$Q^2 = -q^2 = 2EE'(1 - \cos\theta) \qquad , \qquad s = 2mE \qquad (I.2a)$$

where θ is the electron scattering angle in the lab. The momentum–transfer squared, Q^2, is defined to be positive definite, and s is the center–of–mass energy squared. The fractional energy transfer

$$y = \frac{\nu}{E} \qquad (I.2b)$$

is related to the center–of–mass scattering angle of the electron in the electron–target system.

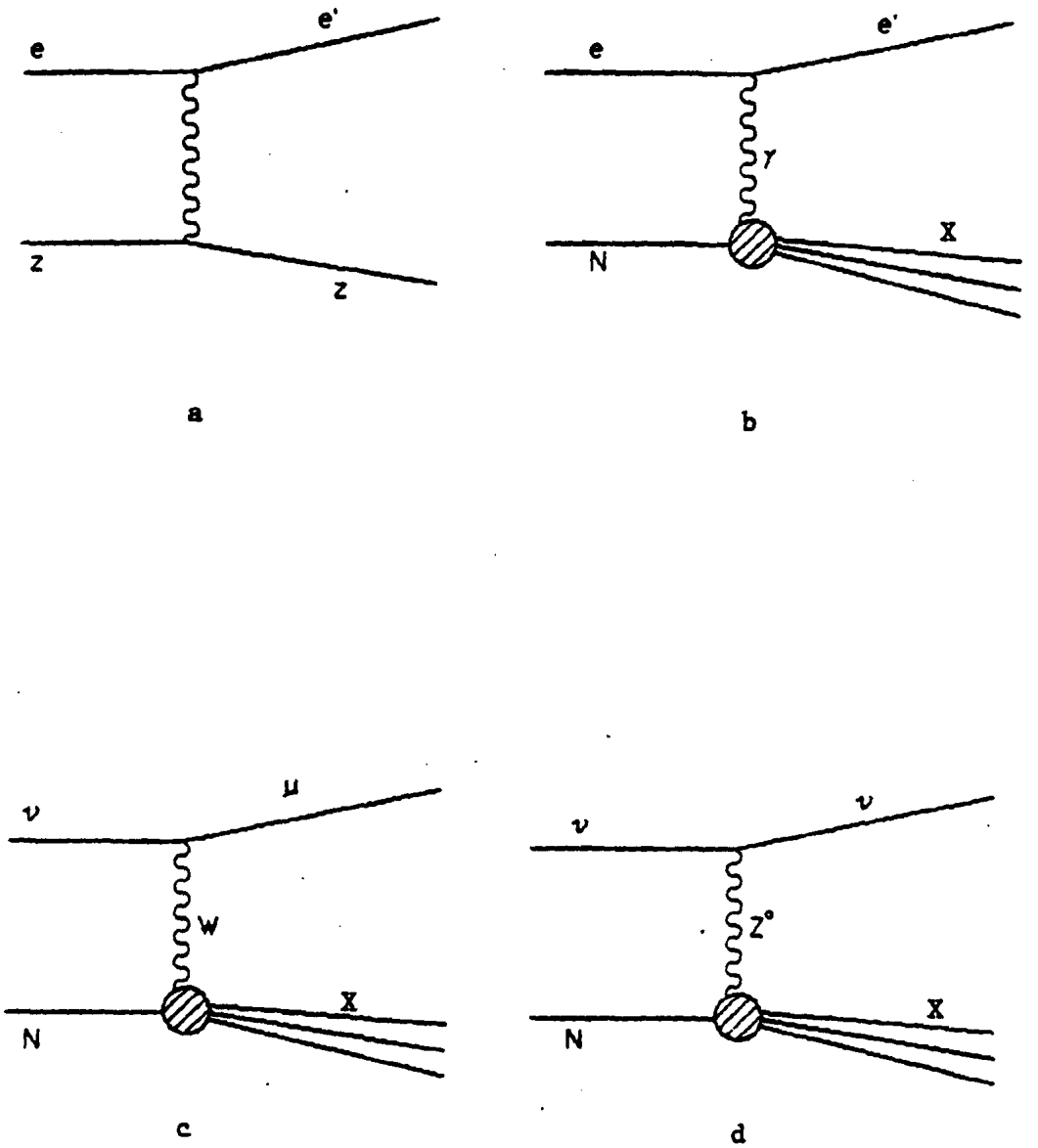

Fig. I.1

The Feynman diagram, in the one–photon exchange approximation, for deep inelastic electron (or muon) scattering off a nucleon

$$e + N \quad \rightarrow \quad e + X \tag{I.3}$$

is shown in Fig. I.1.b.

The differential cross section, as calculated from this diagram, can be written as :

$$\frac{d^2\sigma}{dx\,dy}(e,\mu) = \frac{8\pi\alpha^2 ME}{(Q^2)^2}[\frac{y^2}{2}2xF_1^{(e,\mu)}(x) + (1-y)F_2^{(e,\mu)}(x)] \tag{I.4}$$

The variables Q^2 and y are as defined in Eq. I.2, and

$$x = \frac{Q^2}{2M\nu} \tag{I.5}$$

where M is the mass of the nucleon. $F_1^{(e,\mu)}(x)$ and $F_2^{(e,\mu)}(x)$ are the structure functions of the nucleon. In general, $F_1^{(e,\mu)}$ and $F_2^{(e,\mu)}$ are functions of both x and Q^2. Bjorken[21] conjectured that, in the limit $\nu \rightarrow \infty$, $Q^2 \rightarrow \infty, x$ held fixed, they are functions of only the scaling variable x. This hypothesis agreed with the data to good approximation.[1] It was pointed out by Feynman[3] that the variable x has a very simple physical interpretation in the model in which the nucleon consists of quasi–free point-like particles, called "partons". At very high energies, and in the center–of–mass frame of the lepton–nucleon system

(the "infinite momentum frame"), the observed x is the fraction of the nucleon's momentum initially carried by the parton involved in the scattering.

The two structure functions may be related to the photoabsorption cross sections for transverse photons σ_T and longitudinally polarized photons σ_L.[22] The ratio of the longitudinal to transverse photoabsorption cross sections

$$R = \frac{\sigma_L}{\sigma_T}$$

becomes, in terms of the structure functions,

$$R = \frac{F_2(x)\left(1 + \frac{4M^2x^2}{Q^2}\right) - 2xF_1(x)}{2xF_1(x)} \tag{I.6}$$

For spin $\frac{1}{2}$ partons, $\sigma_L \approx 0$ and $R \approx 0$, since the electromagnetic current conserves helicity. For scalar partons, $\sigma_T \approx 0$, and $R \to \infty$. The experimentally observed small value of R indicates that the partons are spin $\frac{1}{2}$ constituents. At high Q^2 (greater than 10), the Callan–Gross relation,[23]

$$F_2^{(e,\mu)}(x) = 2xF_1^{(e,\mu)}(x) \tag{I.7}$$

is a good approximation to the data.

In the context of the parton model (and as suggested by comparison of Eq. I.1 and Eq. I.4), the cross section $\sigma^{eN}(x)$ for deep inelastic lepton–

nucleon scattering is the sum of the cross sections of the point–like partons, σ_{parton}, each weighted with the probability $f(x)$ of the parton inside the nucleon carrying the fraction x of the nucleon's momentum

$$\sigma^{eN}(x) = \sum_i f_i(x) \quad \sigma_{parton\,i} \tag{I.8}$$

The structure function $F_2^{(e,\mu)}(x)$ can be identified as the sum of the momentum distributions of the partons weighted by the charge squared of each parton, i.e.,

$$F_2^{(e,\mu)}(x) = \sum_i e_i^2 x f_i(x) \tag{I.9}$$

where e is the charge (in units of the proton charge), while the sum is over all partons.

The quark model[24] had been successful in describing the spectrum of hadrons. If the partons had the properties of the quarks, then, for electron scattering off proton and neutron respectively,

$$F_2^{(ep)} = \frac{4}{9}x[u(x) + \overline{u}(x)] + \frac{1}{9}x[d(x) + \overline{d}(x) + s(x) + \overline{s}(x)] \tag{I.10}$$

$$F_2^{(en)} = \frac{4}{9}x[d(x) + \overline{d}(x)] + \frac{1}{9}x[u(x) + \overline{u}(x) + s(x) + \overline{s}(x)] \tag{I.11}$$

where $u(x)$, $d(x)$, and $s(x)$ are the probability distributions in the proton for "up", "down", and "strange" quarks, respectively, and similarly

$\overline{u}(x), \overline{d}(x)$, and $\overline{s}(x)$ are for the antiquarks. The proton and the neutron form an isotopic spin doublet, i.e. their interactions are the same aside from the electric charge. In the "Standard Model", this is reflected by the association of the u–quark and the d–quark in an isospin doublet, as described in section I.2. Thus, in Eq. $I.11$, the following assumptions have been made, on the basis of isotopic spin invariance,

$$\begin{aligned} u(x) &= u^{proton}(x) = d^{neutron}(x) \\ d(x) &= d^{proton}(x) = u^{neutron}(x) \\ s(x) &= s^{proton}(x) = s^{neutron}(x) \end{aligned} \qquad (I.12)$$

and similarly for antiquarks.

If the partons carry all the momentum of the nucleon, then the sum of the fractional momenta should be 1 :

$$\sum_i \int_0^1 x f_i(x)\, dx = 1 \qquad (I.13)$$

Experimentally, from the proton and the neutron structure functions,

$$\sum_i \int_0^1 x f_i(x)\, dx = .48 \pm .02 \qquad (I.14)$$

The deep inelastic electron scattering data indicated that about 50% of the momentum of the nucleon is carried by neutral constituents, conjectured to be gluons.

I.2 Standard Theory of Electromagnetic, Weak and Strong Interactions

Extensive reviews of the gauge theories of the electromagnetic, weak, and strong interactions can be found in the literature.[25] Aspects of the theory relevant to this thesis are described in this section.

In the standard theory of electromagnetic and weak interactions nature's most fundamental fermions are classified into three generations of leptons and quarks :

$$\begin{array}{cccc} \begin{pmatrix} \nu_e \\ e \end{pmatrix}_L & \begin{pmatrix} \nu_\mu \\ \mu \end{pmatrix}_L & \begin{pmatrix} \nu_\tau \\ \tau \end{pmatrix}_L & I = \frac{1}{2} \\ e_R & \mu_R & \tau_R & I = 0 \end{array} \qquad (I.15)$$

for the lepton sector, and

$$\begin{array}{cccc} \begin{pmatrix} u \\ d' \end{pmatrix}_L & \begin{pmatrix} c \\ s' \end{pmatrix}_L & \begin{pmatrix} t \\ b' \end{pmatrix}_L & I = \frac{1}{2} \\ u_R \quad d_R & c_R \quad s_R & t_R \quad b_R & I = 0 \end{array} \qquad (I.16)$$

for the quark sector. The left–handed components in each generation form doublets with weak isospin (I) $\frac{1}{2}$, and the right–handed singlets have isospin 0 .

The basic cross section for a neutrino of incident energy E scattering off a point–like particle of mass m via the charged current, is

$$\frac{d\sigma}{dy} = \frac{G^2 s}{\pi} \qquad (I.17a)$$

while the cross section for an antineutrino is

$$\frac{d\sigma}{dy} = \frac{G^2 s}{\pi}(1-y)^2 \qquad (I.17b)$$

The basic neutrino–quark cross sections $\frac{d\sigma}{dy}$, in units of

$$\frac{G^2 s}{\pi}$$

for the charged current are the following :

$$\begin{array}{lcll} \nu d & \rightarrow & \mu^- x & 1 \\ \nu s & \rightarrow & \mu^- x & 1 \\ \nu \bar{u} & \rightarrow & \mu^- x & (1-y)^2 \\ \nu \bar{c} & \rightarrow & \mu^- x & (1-y)^2 \\ \bar{\nu} \bar{d} & \rightarrow & \mu^+ x & 1 \\ \bar{\nu} \bar{s} & \rightarrow & \mu^+ x & 1 \\ \bar{\nu} u & \rightarrow & \mu^+ x & (1-y)^2 \\ \bar{\nu} c & \rightarrow & \mu^+ x & (1-y)^2 \end{array} \qquad (I.19)$$

and for the neutral current are :

$$\begin{array}{lcll} \nu u & \rightarrow & \nu u & [(+\frac{1}{2} - \frac{2}{3}\sin^2\theta_w)^2 + (-\frac{2}{3}\sin^2\theta_w)^2(1-y)^2] \\ \nu d & \rightarrow & \nu d & [(-\frac{1}{2} + \frac{1}{3}\sin^2\theta_w)^2 + (+\frac{1}{3}\sin^2\theta_w)^2(1-y)^2] \\ \nu s & \rightarrow & \nu s & [(-\frac{1}{2} + \frac{1}{3}\sin^2\theta_w)^2 + (+\frac{1}{3}\sin^2\theta_w)^2(1-y)^2] \\ \nu c & \rightarrow & \nu c & [(+\frac{1}{2} - \frac{2}{3}\sin^2\theta_w)^2 + (-\frac{2}{3}\sin^2\theta_w)^2(1-y)^2] \\ \bar{\nu} u & \rightarrow & \bar{\nu} u & [(-\frac{2}{3}\sin^2\theta_w)^2 + (+\frac{1}{2} - \frac{2}{3}\sin^2\theta_w)^2(1-y)^2] \\ \bar{\nu} d & \rightarrow & \bar{\nu} d & [(+\frac{1}{3}\sin^2\theta_w)^2 + (-\frac{1}{2} + \frac{1}{3}\sin^2\theta_w)^2(1-y)^2] \\ \bar{\nu} s & \rightarrow & \bar{\nu} s & [(+\frac{1}{3}\sin^2\theta_w)^2 + (-\frac{1}{2} + \frac{1}{3}\sin^2\theta_w)^2(1-y)^2] \\ \bar{\nu} c & \rightarrow & \bar{\nu} c & [(-\frac{2}{3}\sin^2\theta_w)^2 + (+\frac{1}{2} - \frac{2}{3}\sin^2\theta_w)^2(1-y)^2] \end{array} \qquad (I.20)$$

I.3 Predictions for Deep Inelastic Neutrino Scattering

The quark–parton model, together with the standard theory of electromagnetic and weak interactions, makes definite predictions for the nucleon structure as probed by the neutrino. These predictions are

described for the charged current and the neutral current, respectively, in the next two sections.

I.3.1 Charged Current

The differential cross section for Deep Inelastic Neutrino Scattering off a nucleon via the weak charged current

$$\nu + N \quad \rightarrow \quad \mu + X \tag{I.21}$$

as calculated from the Feynman diagram shown in Fig. 1.1.c, may be written as :

$$\frac{d^2\sigma}{dx\,dy}\begin{pmatrix}\nu\\ \bar{\nu}\end{pmatrix} = \frac{G^2 ME}{\pi}[(1-y+\frac{y^2}{2})F_2^{CC}(x) \pm (y-\frac{y^2}{2})xF_3^{CC}(x)] \tag{I.22}$$

where $F_2^{CC}(x)$ and $xF_3^{CC}(x)$ are the charged current structure functions, and we have assumed the scaling hypothesis and the Callan-Gross relation Eq. I.7 . For the purpose of comparison between the neutral current and the charged current structure functions, these assumptions will not affect our conclusions.

At present accelerator energies, the neutrino scattering cross section (Eq. I.22) rises linearly with incident energy while the electron scattering cross section (Eq. I.4) is dominated by the $\frac{1}{(Q^2)^2}$ behavior. The structure function $xF_3^{(e,\mu)}(x)$ is absent in the electromagnetic cross section due to

parity–conservation. The $xF_3^{CC}(x)$ term reflects the vector–axial vector interference and is positive for neutrino scattering and negative for antineutrino scattering.

The differential cross section for neutrino scattering off a nucleon is the sum of the basic neutrino–quark cross sections Eq. I.19. The differential cross section per nucleon for neutrino scattering off an isoscalar target, such as the deuteron, can be expressed as the average of the neutrino–proton and neutrino–neutron cross sections.

Comparing Eq. I.22 with the sum of the basic neutrino–quark cross sections, we see that, for any isoscalar target,

$$\begin{aligned} F_2^{CC}(x)^{\nu} &= x[q(x) + \bar{q}(x) + (s(x) - \bar{s}(x) - c(x) + \bar{c}(x))] \\ xF_3^{CC}(x)^{\nu} &= x[q(x) - \bar{q}(x) + (s(x) + \bar{s}(x) - c(x) - \bar{c}(x))] \\ F_2^{CC}(x)^{\bar{\nu}} &= x[q(x) + \bar{q}(x) - (s(x) - \bar{s}(x) - c(x) + \bar{c}(x))] \\ xF_3^{CC}(x)^{\bar{\nu}} &= x[q(x) - \bar{q}(x) - (s(x) + \bar{s}(x) - c(x) - \bar{c}(x))] \end{aligned} \tag{I.23}$$

where

$$q(x) \equiv u(x) + d(x) + s(x) + c(x)$$

$$\bar{q}(x) \equiv \bar{u}(x) + \bar{d}(x) + \bar{s}(x) + \bar{c}(x) \,. \tag{I.24}$$

Henceforth, $c(x)$ is explicitly included for completeness; its contribution is small. Contributions from the more massive quarks are negligible.

Experimentally, the structure functions $F_2^{CC}(x)$ and $xF_3^{CC}(x)$ are obtained from the sum and the difference, respectively, of the neutrino

and antineutrino cross sections. Thus,

$$\begin{aligned} F_2^{CC}(x) &= x[q(x) + \bar{q}(x)] \\ xF_3^{CC}(x) &= x[q(x) - \bar{q}(x)] \end{aligned} \qquad (I.25)$$

$xF_3^{CC}(x)$ corresponds to the momentum distribution of the valence quarks, while $F_2^{CC}(x)$ corresponds to the momentum distribution of all quarks and antiquarks (valence + sea), and can be related (compare with Eq. I.10 and Eq. I.11) to $F_2^{(e,\mu)}(x)$ by :

$$F_2^{(e,\mu)}(x) = \frac{5}{18}F_2^{CC}(x) - \frac{3}{18}[s(x) + \bar{s}(x) - c(x) - \bar{c}(x)] \qquad (I.26)$$

High statistics charged current data exist,[6]. However, there are discrepancies in the total cross sections and structure functions as measured by different experiments, indicating that the systematic errors in absolute normalization are still at the 10% level. To this accuracy, the data are in good agreement with the quark–parton model predictions described in this section.

The charged current data compliment the electron scattering data. They confirm the fractionally charged spin $\frac{1}{2}$ nature of the constituents of the nucleon. Furthermore, experimentally,

$$\int_0^1 F_2^{CC}(x)\, dx = 0.45 \pm 0.02 \qquad (I.27)$$

The charged current data thus indicate that the constituents not interacting with the electromagnetic current also do not interact with the

weak charged current.

In the next section, we will describe the standard model predictions for the main goal of this experiment : the study of the structure of the nucleon using the neutral current.

I.3.2 Neutral Current

The differential cross section for Deep Inelastic Neutrino Scattering off a nucleon via the weak neutral current

$$\nu + N \quad \rightarrow \quad \nu + X \tag{I.28}$$

as calculated from the Feynman diagram shown in Fig. 1.1.d, may be written as :

$$\frac{d^2\sigma}{dx\,dy}\begin{pmatrix}\nu\\ \overline{\nu}\end{pmatrix} = \frac{G^2ME}{\pi}[(1-y+\frac{y^2}{2})F_2^{NC}(x) \pm (y-\frac{y^2}{2})xF_3^{NC}(x)] \tag{I.29}$$

where $F_2^{NC}(x)$ and $xF_3^{NC}(x)$ are the neutral current structure functions. This can be compared with the differential cross section for the charged current Eq. I.22.

Upon comparing Eq. I.29 with the sums of the ν –quark cross sections(Eq. I.20), one obtains

$$\begin{aligned} F_2^{NC}(x)^{\nu} &= F_2^{NC}(x)^{\overline{\nu}} \\ &= (u_L^2 + d_L^2 + u_R^2 + d_R^2)x(q(x) + \overline{q}(x)) \\ &\quad + (d_L^2 + d_R^2 - u_L^2 - u_R^2)x[s(x) + \overline{s}(x) - c(x) - \overline{c}(x)] \qquad (I.30) \\ xF_3^{NC}(x)^{\nu} &= xF_3^{NC}(x)^{\overline{\nu}} \\ &= (u_L^2 + d_L^2 - u_R^2 - d_R^2)x(q(x) - \overline{q}(x)) \end{aligned}$$

where u_L, d_L, u_R, d_R are the neutral current couplings (Eq. I.18) for the left–handed doublets and the right–handed singlet components of the quarks(Eq. I.16), and are shown explicitly in Eq. I.20.

For a direct comparison of the neutral current and the charged current interactions, we define $R(x,y)$ to be the ratio of the double differential cross sections, thus

$$\begin{aligned} R(x,y) &= \frac{\frac{d^2\sigma}{dx\,dy}^{NC}}{\frac{d^2\sigma}{dx\,dy}^{CC}} \\ &= \frac{(1-y+\frac{y^2}{2})F_2^{NC}(x) \pm (y-\frac{y^2}{2})xF_3^{NC}(x)}{(1-y+\frac{y^2}{2})\,F_2^{CC}(x) \pm (y-\frac{y^2}{2})\,xF_3^{CC}(x)} \end{aligned} \tag{I.31}$$

where $\pm$ should be replaced by $+$ for neutrinos, and $-$ for antineutrinos. We shall adopt the convention that this ratio be specified by $\overline{R}(x,y)$ for antineutrinos, and $R(x,y)$ for neutrinos.

$R(x,y)$ and $\overline{R}(x,y)$ are independent of the flux and other absolute normalization factors. Furthermore, because they are ratios of double differentials, they can be tested in any finite (x,y) kinematic region. Using $R(x,y)$ and $\overline{R}(x,y)$, we shall determine the momentum distributions $x[q(x)+\overline{q}(x)]$ and $x[q(x)-\overline{q}(x)]$ in Eq. I.30 (which we shall call $\tilde{F}_2^{NC}(x)$ and $x\tilde{F}_3^{NC}(x)$ respectively) from the neutral current events, and compare with $F_2^{CC}(x)$ and $xF_3^{CC}(x)$.

Thus, $R(x,y)$ and $\overline{R}(x,y)$ provide an extensive test for the Standard Model predictions. The momentum x distribution of the quark–partons as probed by the neutral current can be compared directly with the distribution as probed by the charged current. Whether the weak neutral current sees the same constituents inside the nucleon as does the weak charged current is an important test of the validity of the Standard Model.

II. The Neutrino Beam

The high energy neutrinos in this experiment were obtained from the neutrino narrow band beam at Fermilab. High energy neutrino beams from modern particle accelerators in general are of the following three types :

1.The wide band beam. In this type of beam, secondary particles of all momenta of a selected sign are focused to produce the maximum number of neutrinos.

2.The narrow band beam. In this beam, only particles of a small momentum range are focused. The number of neutrinos is down by about 2 orders of magnitude compared to the wide band beam. However, the energy of each neutrino is well defined, and can be determined on an event–by–event basis to about 10%, as described in this chapter.

3.Prompt neutrinos from a beam dump. In a beam dump, the relatively long–lived secondary particles, such as the pion and the kaon, would interact inside the dump, and would not decay into neutrinos. Only the short–lived charm particles, such as the F meson and the D meson, would decay into neutrinos. The primary interest for this type of beam is that it should be a source of tau neutrinos, composing a few percent of the beam, the rest being equal mixture of electron neutrinos

and muon neutrinos.

II.1 Principles of the Narrow Band Beam

In the semi–leptonic neutral current processes where one cannot measure the energy of the outgoing neutrino, it is neccessary to know the energy of the incident neutrino. This can be achieved by focusing and collimating pions and kaons with momenta in a narrow and well measured range. From simple two body decay kinematics, for a particle of momentum P_0 and mass m decaying into a muon and a neutrino, we can determine the energy of the neutrino as follows :

$$E_\nu = \frac{m^2 - \mu^2}{P_0\theta_\nu^2 + m^2/P_0} \qquad (II.1)$$

where θ_ν is the decay angle of the neutrino with respect to the secondary particles (pions or kaons), and μ is the mass of the muon. In the experiment, this decay angle for each event is determined from the radial distance of the vertex from the beam axis. Furthermore, for spin 0 particles such as the pion and the kaon, the decay is isotropic in the rest frame. For a monochromatic beam, the neutrino energy spetrum would be flat between 0 and the maximum energy $P_0(1 - \mu^2/m^2)$.

In nearly 100 % of the decay of the pion and in 63.5 % of the decay of the kaon, (the $K_{\mu 2}$ mode), the decay products are a muon and

a neutrino. The energy versus radius correlations for neutrinos from π and $K_{\mu 2}$ decays respectively, as obtained from a beam Monte Carlo simulation, are shown in Fig. II.1.a and Fig. II.1.b. In other decay modes of the kaon with more than two particles in the final state, a neutrino may be produced with an associated muon ($K_{\mu 3}$ decay) or electron (K_{e3} decay). The energy versus radius distributions for neutrinos from $K_{\mu 3}$ and K_{e3} decays, respectively, are shown in Fig. II.1.c and Fig. II.1.d.

The energy resolution of the incident neutrino at a radius r_0 from the beam center is determined by several factors :

1.the finite momentum bite of the dichromatic train

2.the angular divergence of the beam

3.the uncertainty of the decay position in the decay pipe.

II.2 Fermilab Narrow Band Beam

The experiment used the Fermilab Narrow Band Beam. Primary 400 GeV/c protons were directed to a 12 inch long BeO target. The produced secondary particles were momentum and sign selected to form a mono-energetic beam of particles, composed of mostly pions, kaons and protons. The data in this analysis were taken with the secondary momentum set to +165, +200, +250 and −165 GeV/c.

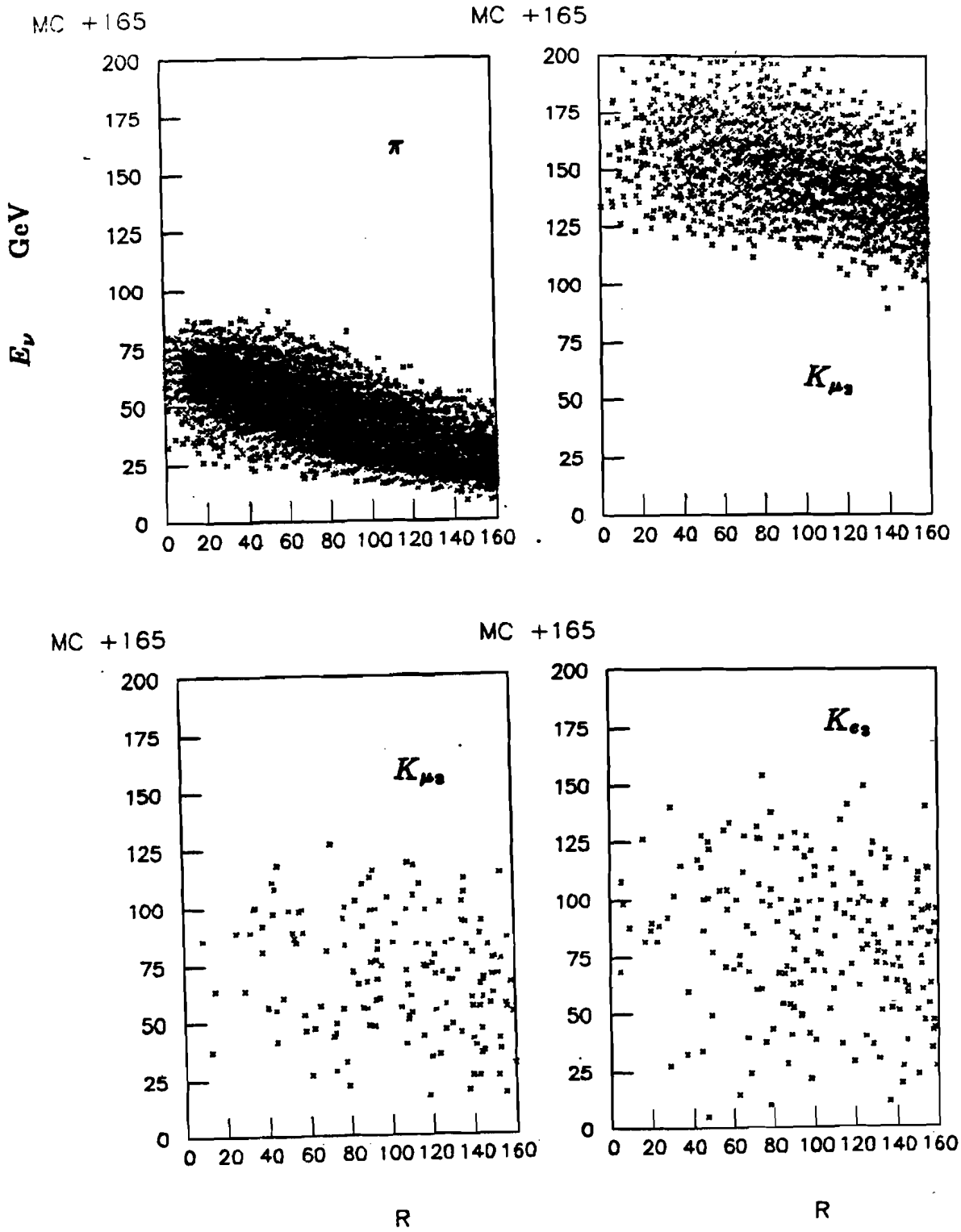

Fig. II.1 E_ν versus radius

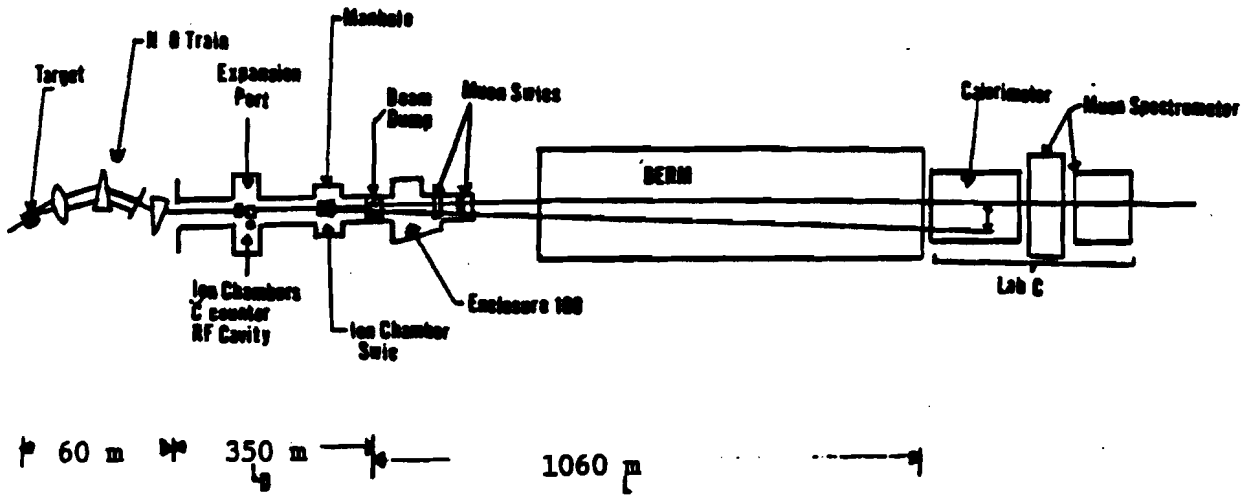

Fig. II.2 Layout of Fermilab Narrow Band Beam

The layout of Fermilab Narrow Band Beam is shown in Fig. II.2. The secondary particles are allowed to decay in a 352 meter long decay tunnel, which is followed by 1066 meters of earth and iron shield, allowing a beam of $\simeq 100\%$ neutrinos to reach Lab C.

II.3 Beam Monitors for Total Secondary flux

Beam flux monitoring is crucial for total cross section and other analyses that require absolute normalization. Since the present analysis is independent of flux, the beam monitors are briefly described for completeness. Detailed description can be found in the references[26].

The total number of protons on target were monitored by a beam

current transformer, a secondary emission monitor, and a R. F. cavity. The total number of momentum selected secondary particles were monitored by two ion chambers and a R. F. cavity. The monitors were calibrated using 200 GeV/c ($\pm 1\%$) protons transported to the train from the main ring. Typically, each monitor determines the beam intensity to a few percent. In addition, two segmented wire ionization chambers monitor the secondary beam shape and position, corresponding to about 3 cm accuracy in the lateral beam position determination at Lab. C.

II.4 Cerenkov Counter Pressure Curve

The fraction of each type of particle and the average momentum are obtained from measurements[27] employing a differential Cerenkov counter which is described in detail elsewhere.[26]

II.4.1 Average Momentum

The momentum of a particle can be determined from the angle of Cerenkov light emitted by the particle

$$\theta_c = [2kR - \frac{m^2}{P^2}]^{1/2} \qquad (II.2)$$

where $2k = 8.615 \times 10^{-8}$ /Torr is the gas constant, R is the pressure(in Torr), P is the momentum(GeV/c), and m is the mass (GeV/c^2). The index of refraction and the gas constant are calibrated using 200 GeV/c

primary protons.

The momentum scale of the narrow band beam is determined to within 1 % using the proton peak in the Cerenkov curve.

II.4.2 Particle Fraction

The particle fraction is proportional to the area in the Cerenkov counter output versus pressure curve in Fig. II.3. Particle Fractions at the end of the momentum selection train are shown in the following table :

P_0	π	K	p
GeV/c	%	%	%
+165	$29.2 \pm .3$	$4.2 \pm .2$	$66.6 \pm .6$
+200	$18.9 \pm .2$	$2.8 \pm .1$	$78.2 \pm .2$
+250	$7.8 \pm .1$	$1.3 \pm .1$	$90.9 \pm .2$
−165	$90.0 \pm .4$	$5.9 \pm .3$	$1.2 \pm .3$

II.5 Flux Calculation from Monte Carlo Simulation

The information obtained from the beam monitors are incoporated in a computer program that calculates the neutrino beam flux. This includes the momentum bite, the beam divergence, the number of secondary particles, and the particle fractions.

The pions and the kaons are then allowed to decay to produce neutrinos, constrained only by the length of the decay pipe. All decay

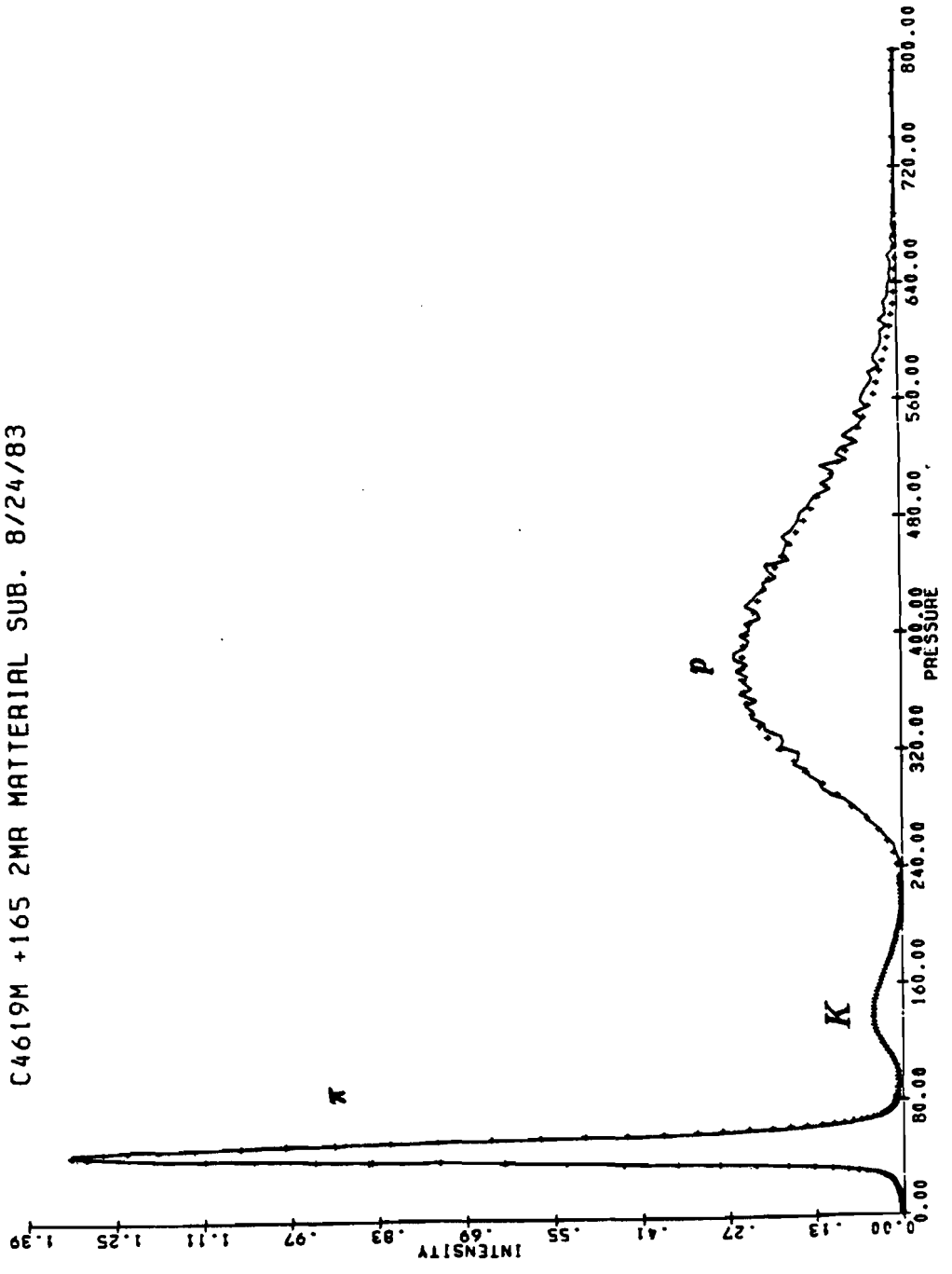

Fig. II.3 Cerenkov pressure

modes have been taken into account.

This beam monte carlo creates a file of neutrinos for each momentum setting of the secondary particles. The energy, decay process (π, K_{μ_3}, K_{μ_3}, or K_{e_3}), and the lateral position relative to the beam center at Lab C are provided for each neutrino. These neutrinos are then used in the complete monte carlo calculations and event simulations for the detector.

III. The Lab C Detector

The Lab C[28] detector was designed and built for the study of high energy neutrino interactions. Our primary goal has been to study the neutral current interaction

$$\nu + N \rightarrow \nu + X$$

and compare with the charged current interaction

$$\nu + N \rightarrow \mu + X$$

To meet this goal, it is important that the detector has the following properties :

1.A large mass to yield a large number of events.

2.Fine granularity so that both the energy and angle of the hadron shower can be measured well.

3.Pattern recognition capability to ensure identification of the muon for charged current events.

4.The ability to measure the momentum of the muon for the traditional charged current analysis.

The Lab C detector consists of a target–calorimeter and a muon spectrometer to provide the above properties. The schematic layout of the Lab. C detector is shown in Fig. III.1.

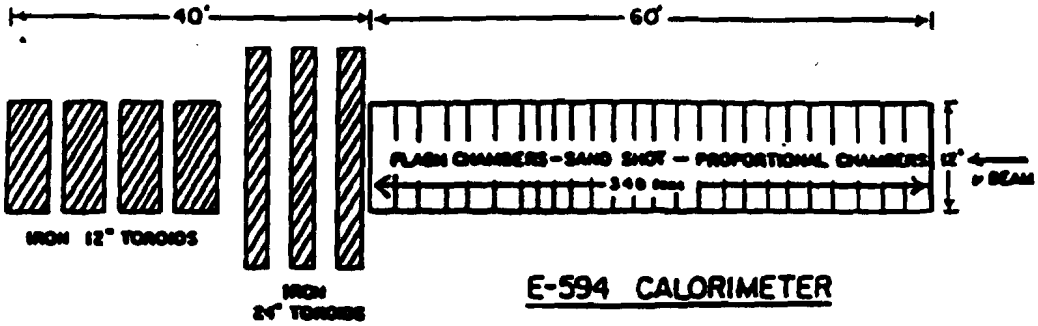

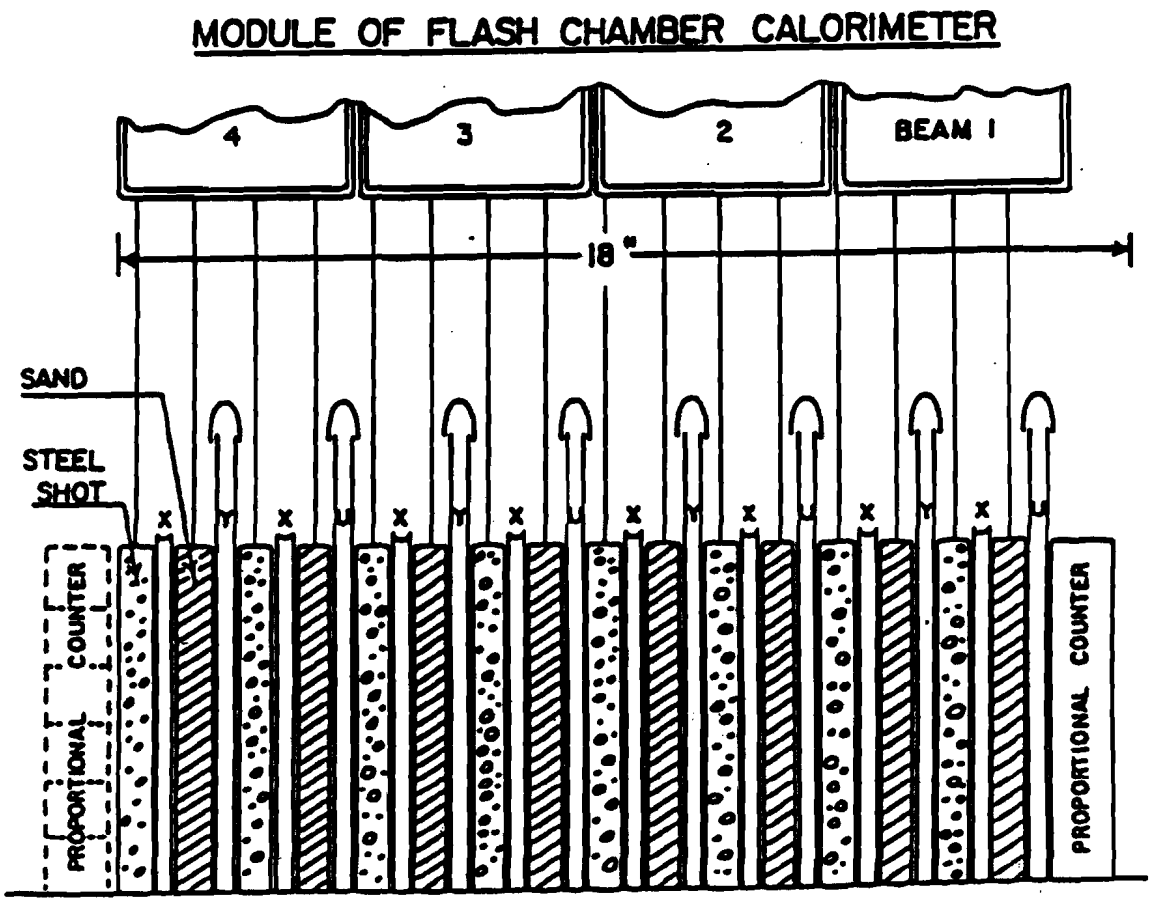

Fig. III.1 schematic of the E594 detector

III.1 The Calorimeter

The calorimeter consists of 38 modules of flash chambers, proportional tube chambers, and sand and steel shot target planes. The structure of a module of the calorimeter is shown in Fig. III.1. The module consists of 4 units of 4 flash chambers (U,X,Y,X) positioned between $\frac{5}{8}$ inch plastic extrusions which are alternately filled with sand and steel shot, followed by one proportional tube chamber. The average separation between flash chambers is 3 cm. The flash chambers in the three views (X, Y, and U) have cells at angles (0., 80., and 100.) degrees with respect to the horizontal plane, respectively. Thus, there are a total of 608 flash chambers, 37 proportional tube chambers, 304 sand target planes, and 304 steel shot target planes, with a total weight of $\approx$ 340 metric tons. The weight of the detector for any fiducial volume is known to $\pm$ 3 %. The average density of the calorimeter is 1.4 g/cm^3, and the average Z is 21. The flash chambers sample every .22 radiation length, and every .03 absorption length.

Each flash chamber is constructed from three 4′–wide sheets of extruded polyproplyene, with 5. mm $\times$ 5.9 mm cells, having an active area of 12′ by 12′. A gas mixture of 90 % Neon and 10 % Helium flows through the cells at an operating rate of one volume change per hour.

Electrodes of 5 mil aluminum foil are glued to both sides of the polyproplyene sheet. When a trigger is made by the proportional tube chambers, a high voltage pulse is applied to one electrode, creating a high electric field inside the flash chamber cells. The avalanche formed in the cell traversed by a charged particle creates a plasma discharge which propagates along the cell with a speed of 0.1 ft/nsec. The plasma discharge in a hit cell causes the capacitance between the readout strip and the high voltage electrode to change, inducing a current pulse through the copper strips to the ground electrode. The current pulse induced in the sense wire causes an acoustic pulse on a Remendur 27 magnetostrictive wire. The acoustic pulse propagates at 500 m/sec, providing a 1μ sec separation of adjacent hit cells. The magnetostrictive wire is situated inside an aluminum bar, which is surrounded by a solenoidal coil that periodically magnetizes the wire. Amplifiers with gains of 1000 at each end of the magnetostrictive wand provide analog signals for the readout system.

The proportional tube chambers provided the triggers for the events. Each proportional tube chambers is constructed from eighteen 12′ long aluminum extrusions, each with eight 1 in. by 1 in. cells. Each cell is strung with a 50 μm gold plated tungsten wire, for a total of 144 wires

per plane. A positive voltage of 1650 volts is applied on the wire. Each plane is instrumented with 36 charge amplifiers,[29] each connected to 4 consecutive wires. A gas mixture of 90 % Argon and 10 % methane flows through the cells at an operating rate of 0.5 cubic ft. per hour per plane.

Each amplifier provides a "Fast Out" analog signal. The Fast Out from the 36 channels is added to give "Sum Out" for each plane. "Sum Sum", the sum of Sum Outs from the 37 planes, is a measure of the total energy deposition in the calorimeter, and provides a fast trigger for the detector. "Analog Multiplicity" is a signal with an amplitude proportional to the number of Fast Outs above a discriminator level within a plane.

In addition, each amplifier provides a "Slow Out" signal which is delayed and sampled by a track and hold circuitry. This is read out by a scanner, and the digitized information is transmitted via a CAMAC crate to a PDP-11 computer, in which the information is both used for on-line analysis and stored on tapes.

The on-line analysis monitored the performance of each chamber, the beam, the triggering, and the entire data taking process. Off-line programs were able to monitor this information in more detail and to reconstruct each event within few hours after the event was taken.

III.2 The Muon Spectrometer

In order to measure the momentum of the muon from a charged current interaction, the target–calorimeter is followed immediately by a muon spectrometer.[30] The schematic of the muon spectrometer is shown in Fig. III.2.

The spectrometer consists of three 24′ diameter iron toroids and four 12′ diameter iron toroids. Each 24′ toroid is composed of three slabs of donut–shaped iron, of a thickness of 20 cm. Each 12′ toroid is composed of 6 slabs of donut–shaped iron with the same thickness of 20 cm. The gaps between the toroids are instrumented with proportional tube planes, of similar construction to the ones in the calorimeter. The differences are : 1. Cell lengths of 12′, 16′, and 24′ are used here to cover the larger areas necessary for acceptance. 2. The extrusions are two cells in thickness, such that each proportional tube plane gives two independent measurement of one coordinate (x or y) of the muon, with a $\frac{1}{2}$ inch offset between the two measurements.

A positive voltage of 1950 volts is applied on the wire. The wires are read out by a charge division scheme. Series of seven and fifteen resistors are used with resistances of 100 Ω and 68 Ω respectively, between wires, for the eight and the sixteen wire charge division configurations. Two

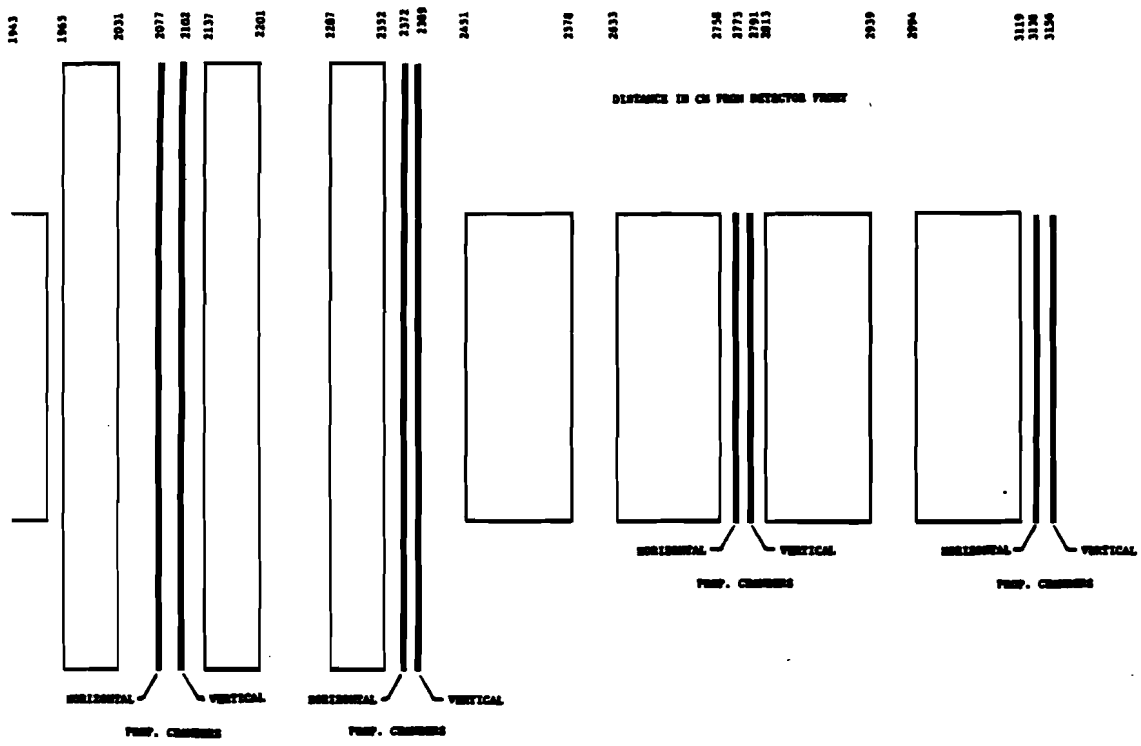

Fig. III.2 schematic of the muon spectrometer

charge amplifiers, identical to the ones used in the calorimeter, are connected to the two ends of a series of resistors. Blocking capacitors are used to separate the signal from the applied voltage.

The charge Q_0 deposited on the wire, within the cell traversed by the muon, divides into Q_1 and Q_2 between the two amplifiers. The difference between the two charges Q_1 and Q_2, normalized by the sum, determines the wire onto which the charge was deposited, and the corresponding cell.

An array of the position measurements located the muon trajectory. Together with the knowledge of the magnetic field, they enabled us to determine the momentum of the muon. The reconstruction of the muon momentum is described in section III. 4.

III.3 Calibration and Resolutions

To convert the response of the detector (such as the total number of hits in the flash chambers, or the pulse height in the proportional chambers) to physical quantities, hadron beams of known momenta were transported to Lab C to calibrate the detector. The nominal calibration momenta were :

5, 10, 20, 35, 50 GeV/c for electrons,

5, 10, 20, 35, 50, 75, 100, 125 GeV/c for hadrons,

20, 40, 50, 75, 100, 125 GeV/c for muons.

From survey information, it was determined that the calibration beam entered the detector horizontally, and at an angle of $68.9 \pm .2$mrad with respect to the line parallel to the center of the detector, which is parallel to the neutrino beam. This is consistent with the angles determined from fitting muon tracks in the calibration beam, which gave $\theta_x = -0.02 \pm .2$mrad, and $\theta_y = 68.5 \pm .1$mrad.

III.3.1 Vertex resolution.

Good vertex resolution is important for determination of the shower angle, and for rejecting (as charged current muon candidates) tracks that do not originate from the vertex.

The vertex of an event is determined from visual scanning, and from the computer routine VRTDRV. Each event picture has been displayed and magnified on a Tektronix CRT terminal to digitize the vertex in each of the three (U,X,Y) views and to classify the event, much like a bubble chamber picture. Vertex finding routines have also been developed.

VRTDRV first uses information from the proportional tube chambers(latch bits) to determine an approximate beginning of the shower. Centroids of flash chamber hits, for 64 chambers in the region, are then fitted to determine the vertex position in each view. The resolution of

the vertex can be determined in the following ways :

A good vertex determination can be made by fitting the incident track of the calibration hadrons, before they interact. Comparison between the vertex so determined and the vertex determined from scanning, shows that the scan vertex resolution for the calibration hadron showers is 2 cm, while the resolution from the routine VRTDRV is 2.5 cm.

By fitting the charged current muon track, in a similar fashion, the vertex resolution for the charged current events is determined to be 2 cm from scanning, and 3 cm from the routine VRTDRV.

Both the incident track for a calibration hadron and the muon track for a charged current event can be removed after fits to these tracks are made. The vertex resolution from the "trackless" scan and from VRTDRV without these tracks are 3 cm. Thus, the scan vertex resolution is slightly better for the charged current event than for a neutral current event, while the VRTDRV program vertex does not have such a bias. However, the shower angular resolution is not sensitive to the difference at this level.

Monte Carlo events with complete shower generation have known vertices, and can be used to measure these resolutions. The resolution from scanning these events is 2 cm, while it is 3 cm from VRTDRV.

Since the flash chambers are arranged in three independent views, there is a constraint equation for any position or angle measurement. This provides a check for the vertex determination, and can be used to improve slightly the hadron angle determination.

The resolution of the vertex is taken to be 3 cm., and is roughly independent of the energy of the shower.

III.3.2 Hadron shower energy.

The flash chamber registers a "hit" due to the ionization of a traversing particle. To the first order, the track length of each particle times the number of particles, thus the number of hits in the detector, is proportional to the total energy of the shower. This response of the detector was calibrated using particles of known momenta that interact in the detector. The number of hits rises linearly with the energy of the shower. In a dense region of the shower, however, due to the finite size of the flash chamber cell, only one hit would be registered in a given cell, even if more than one particle traversed the same cell. Thus, a saturation correction is necessary to linearize the energy–hit relation. In addition, an efficiency correction is needed because the 608 flash chambers are not equally efficient in registering a hit. The efficiency of each chamber is studied using the large number of cosmic ray triggers taken during the

same period the as data.

In a similar fashion, the total pulse height of the proportional tube chambers is proportional to the total energy of the shower. Since the pulse height is an analog signal, no saturation correction is needed. Using the proportional tube chambers alone for energy reconstruction in the detector has the disadvantage that the sampling is coarse, especially for low energy showers.

The shower energy reconstruction routine uses a resolution–weighted mean of the measurements from the flash chamber hits and the proportional chamber pulse heights. The reconstructed hadron shower energy as a function of the incident hadron energy is shown in Fig. III.3.a. The resolution in this energy determination is shown is Fig. III.3.b.

The resolution of the hardon shower energy can be parametrized as :

$$\frac{\sigma(E_{hs})}{E_{hs}} = 0.055 + \frac{0.462}{\sqrt{E_{hs}}} \qquad (III.1)$$

For a neutrino interaction, the reconstructed E_{hs} is the quantity $E_H - M$ in GeV.

To minimize the effects on shower energy and angle determinations, due to noise hits in the detector, only chambers in the region of the

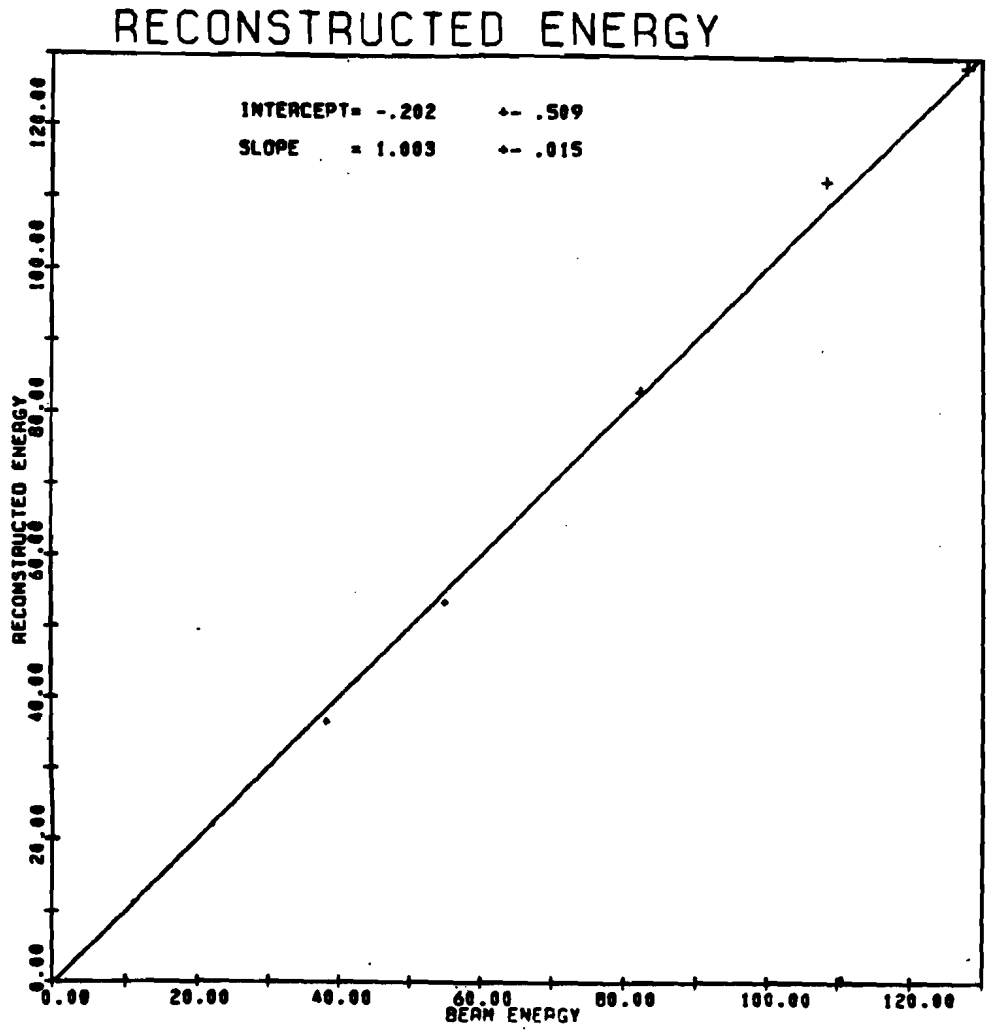

Fig. III.3.a hadron energy

shower are used for these determinations. The region is defined to be between the vertex and JEND, the end of the shower.

To determine JEND, the proportional tube chamber Analog Multiplicity is first used to locate the end of the dense part of the shower. Flash chamber hits are then used to search up to 5 interaction lengths

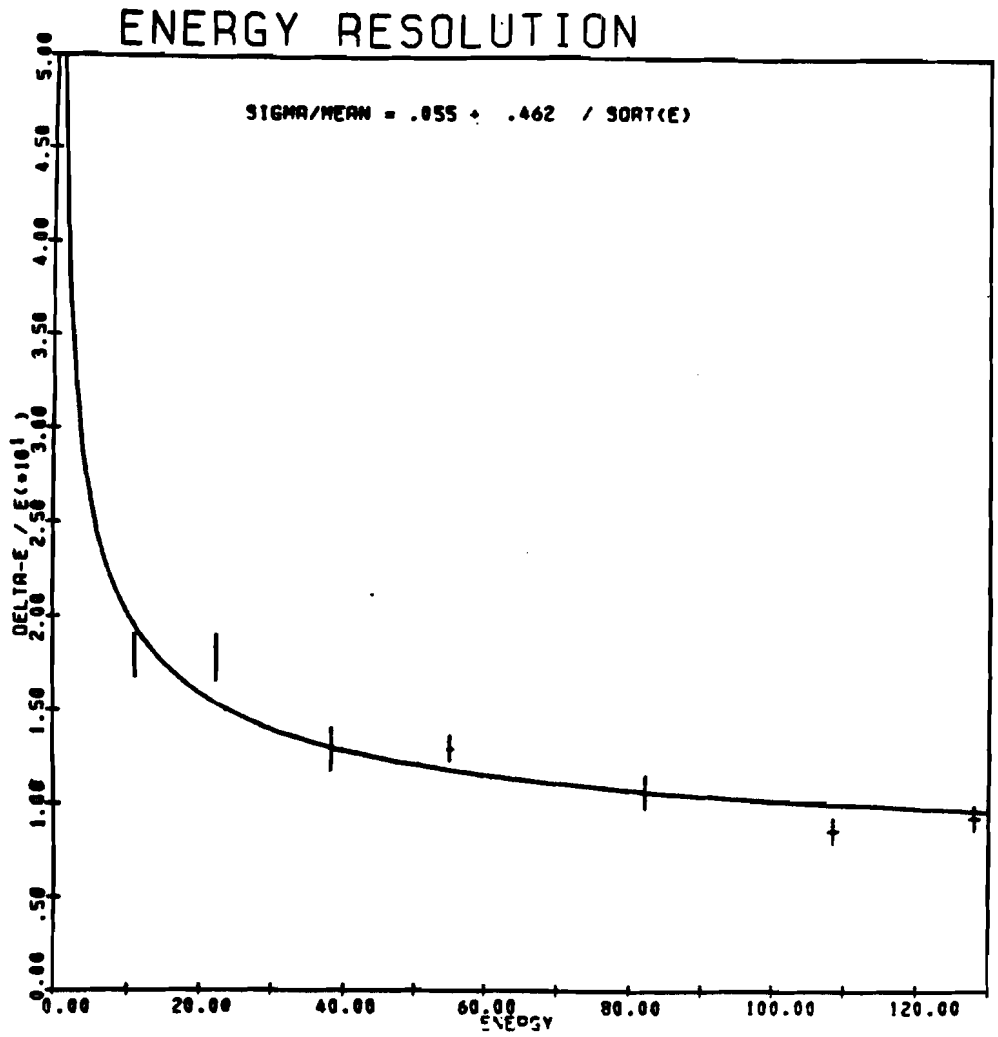

Fig. III.3.b hadron energy resolution

beyond this location, requiring JEND to be the last chamber of the furthest downstream series of 16 chambers with at least 4 hits in each of at least 6 chambers. Comparison between the shower length (JEND – JVERT) for charged current and for neutral current events indicates that there is no bias due to the muon track.

In general, JEND so determined corresponds to where a visual scan would identify the end of the shower. More quantitatively, the total number of hits between JVERT and JEND is 99 % of the total number of hits between JVERT and (JEND + 5 interaction lengths) for shower energies above 35 GeV, and 98 % for lower energies. The difference is due to the number of noise hits relative to shower hits.

To reconstruct the kinematics for the charged current events the same way as for the neutral current events, the muon track is eliminated in the analysis. By superposing muon tracks on neutral current events, we have determined that, with the algorithm for muon identification and elimination, the shower angle measurement is unaffected by the muon track for charged current events. The shower energy determined after the muon track elimination is found to be 0.5 GeV less than the energy of the shower determined prior to the superposition of the track. The effect is small and compensates for the estimated muon internal bremsstrahlung.

III.3.3 Hadron shower angle.

Two major independent algorithms have been developed to reconstruct the hadron shower angle. The routine SHWANG does an angular histogram at the vertex, with an angular range of (−1.4 to 1.4) radians

along the incident beam direction, in bin size of 10 mrad. The mean shower angle is determined by :

$$\theta_{hs} = \frac{\sum_{i=1}^{N} E_i\theta_i}{\sum E_i} \simeq \frac{\sum_{i=1}^{N} n_i\theta_i}{\sum n_i}$$

where E_i and n_i are the energy and the number of hits in the ith bin, respectively, and θ_i is the angle of the ith bin.

The routine HADFLO determines the shower axis by fitting the center of gravity of hits for each flash chamber in the shower region. The weight of each center of gravity is calculated from the number of hits in the chamber and the mean square error of hits from the shower axis from the previous fit iteration. Three iterations are used in the fitting procedure with slightly narrowing cuts to decrease sensitivity to noise hits.

Both methods give the same resolution and mean accuracy in the angle of the hadron calibration beam. In the final analysis, the routine SHWANG was used.

The resolution can be determined from :

$$\begin{aligned} \sigma(\theta_{hs,x}) &= 7.3 + \frac{1008.}{E_H} \quad \text{mrad} \\ \sigma(\theta_{hs,y}) &= 11. + \frac{1064.}{E_H} \quad \text{mrad} \end{aligned} \qquad (III.2)$$

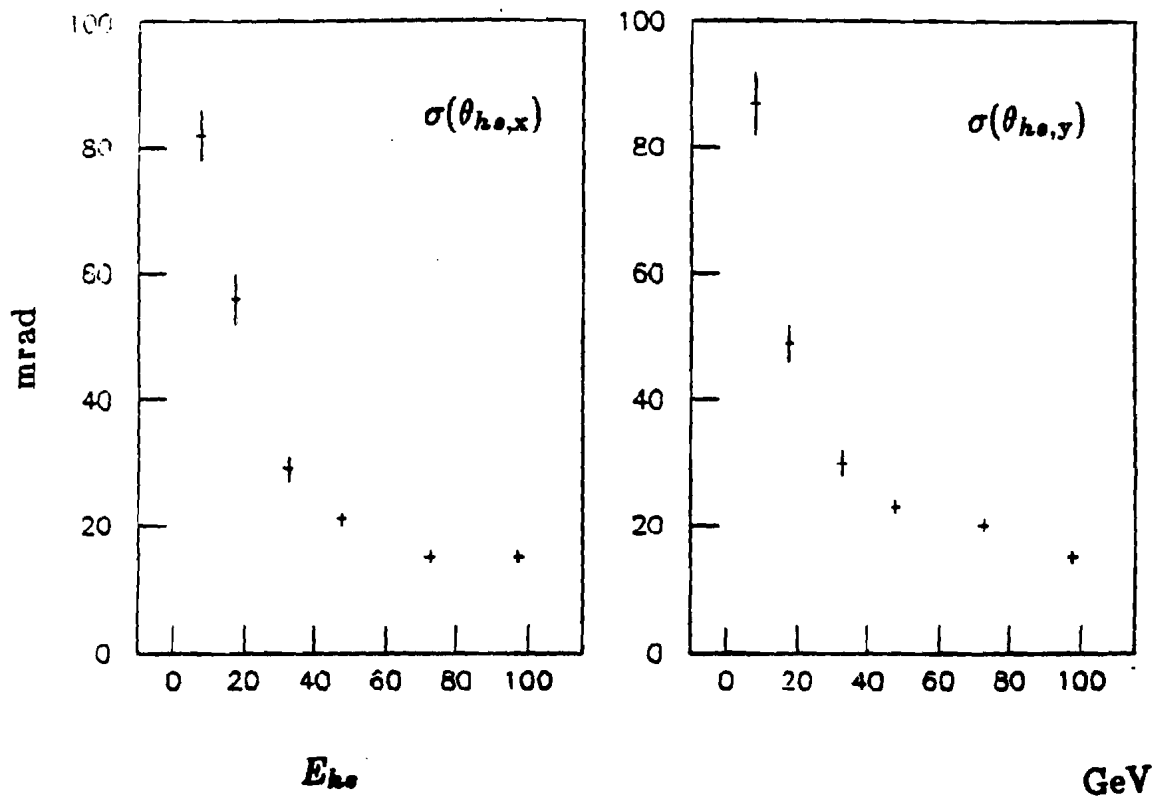

Fig. III.4 hadron anglular resolution

for two orthogonal projections of the angle. The resolutions of the hardon shower angle as a function of the shower energy are shown in Fig. III.4.

Cosmic rays that enter the detector can bremsstrahlung or interact and generate showers along the incident direction. The difference between the shower angle reconstructed and the angle of the incident track indicated that there is little angular bias in the shower angle deter-

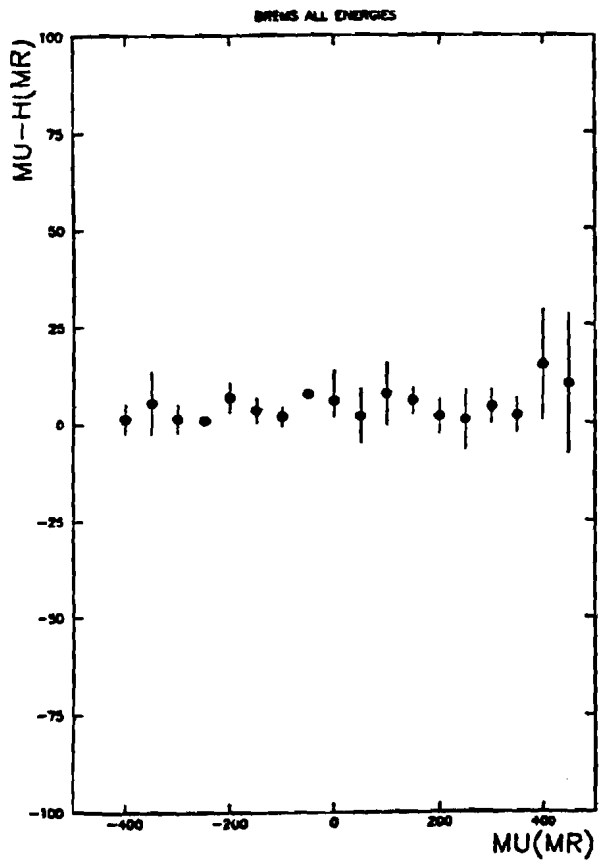

Fig. III.5 $(\theta_{shower} - \theta_{track})$ vs θ_{track}

mination, over a wide range of shower angles, as shown in Fig. III.5.

III.3.4 Muon angle.

For neutrino interactions, the muon angle is the best measured kinematic quantity. The resolution is determined by the uncertainty due to multiple scattering, and by the spatial resolution of the detector. The effective spatial resolution of the Lab C detector, from aligning beam

muons, is determined to be $\simeq \pm$ 0.6 cm for the X flash chambers, and $\simeq \pm$ 0.9 cm for the Y and U chambers. The average distance traversed in the calorimeter by a charged current muon is $\approx$ 1000 cm. The muon angular resolution can be represented by :

$$\sigma(\theta_\mu) = 1.59 + \frac{97.1}{P_\mu} \quad \text{mrad} \qquad (III.3)$$

where P_μ is the muon momentum in GeV/c.

III.3.5 Muon momentum.

For the charged current events, the hadron shower energy, the muon angle, and the muon momentum (E_{hs}, θ_μ, and P_μ, respectively) determine the kinematics of an event. These have been the ingredients for the standard charged current analysis.

All muon candidates in the charged current events have been analyzed by the muon momentum reconstruction routine TRACKM. Employing the knowledge of the magnetic fields in the toroids, iterative maximum likelihood fits are made to the measured positions of flash chamber hits in the calorimeter and the toroid chamber hits to reconstruct the muon momentum. Ionization energy loss and multiple Coulomb scattering are taken into account. Measurements of the magnetic field using a Hall probe are in good agreement with the calculated field.

The average field is $\approx$ 17 kG. The reconstructed muon momentum as a function of the calibration muon beam momentum is shown in Fig. III.6.

A neutrino can interact quasi–elastically with a nucleon, resulting in a muon with nearly all of the energy of the incident neutrino. These events have been studied[31,32] extensively in our detector, and provide a cross check between the incident neutrino energy at a given radius and the muon momentum from a quasi–elastic event at that radius.

The muon momentum resolution can be determined from :

$$\sigma(\frac{1}{P_\mu}) = (\frac{5.1}{l} + (\frac{333.3}{l^2})^2)^{\frac{1}{2}} \frac{1}{P_\mu} \qquad (III.4)$$

where l (in cm) is the thickness of the magnetized iron traversed by the muon.

III.4 Trigger

The proportional tube chambers provided the triggers for the events. The trigger condition requirements were :

More than one proportional tube plane, each with Analog Multiplicity greater than one ; Sum Sum greater than 75 mV ; Front scintillator counter veto against muons and upstream interactions.

The trigger efficiency as a function of the shower energy is shown in Fig. III.7. The trigger efficiency rises linearly with shower energy at

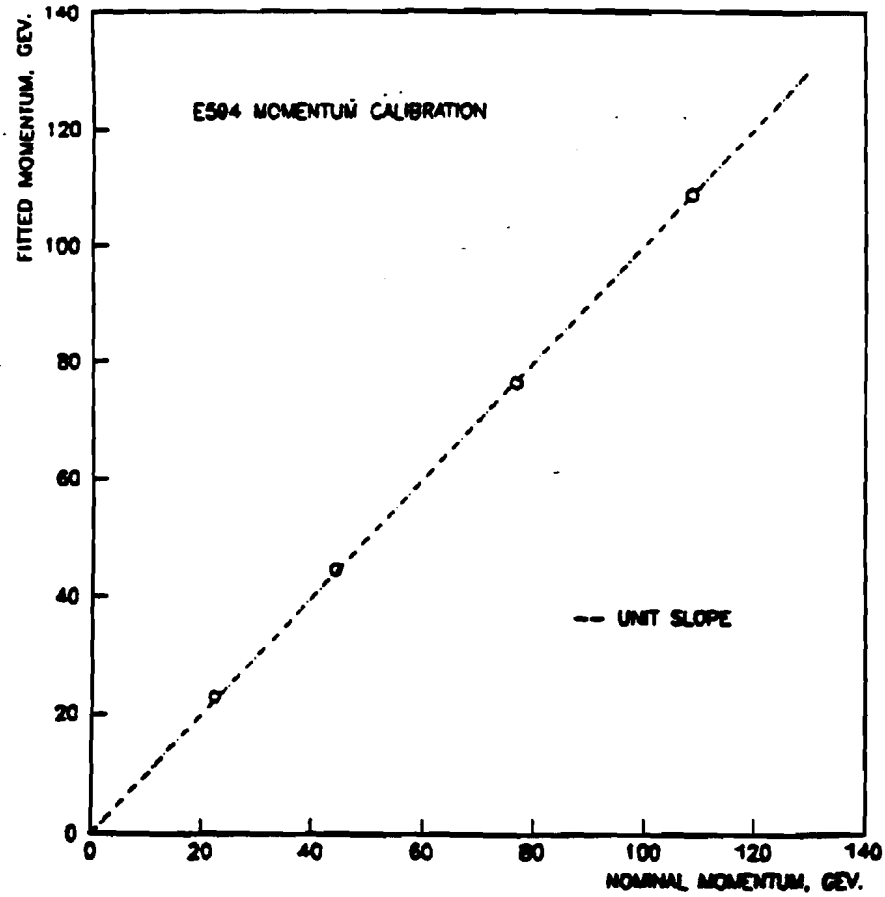

Fig. III.6 muon momentum

low energies, and is $\simeq$ 100% for shower energy above 7 GeV.

The data have been analyzed both with a 10 GeV and with a 15 GeV minimum hadron shower energy cut. The results are independent of the cuts. We are confident that, by requiring the minimum hadron energy to be greater than 10 GeV, both the neutral current events and the charged current events have 100% trigger efficiency.

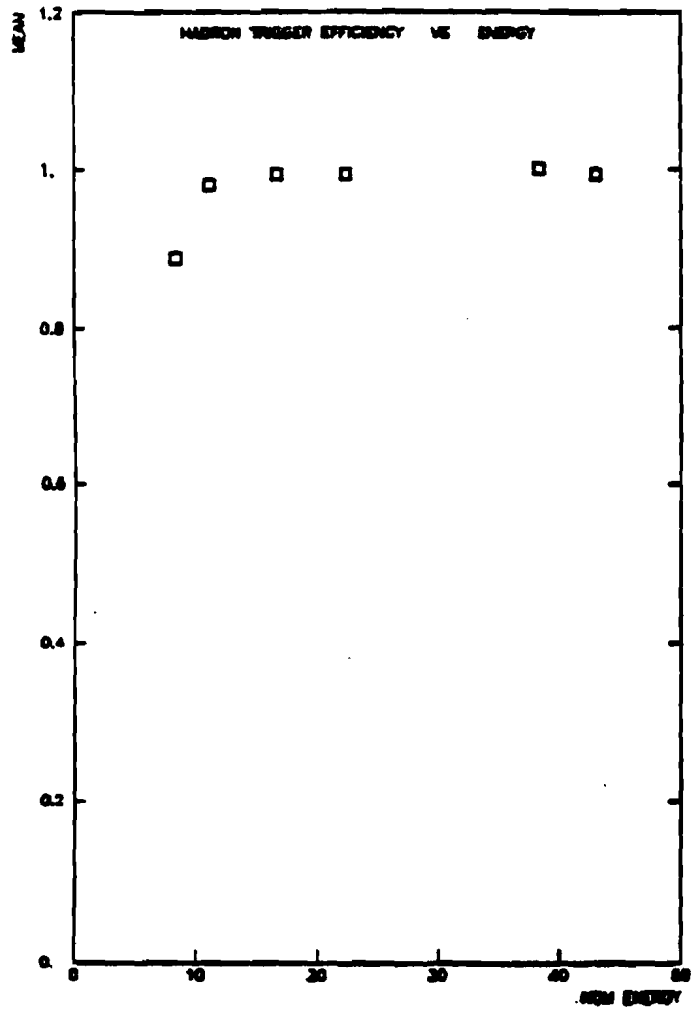

Fig. III.7 trigger efficiency

IV. Event Reconstruction

The process of reconstructing physical quantities for neutral current and charged current events from all triggers is described in this chapter. From visual scanning, and from a complete pattern recognition computer program, cosmic ray triggers have been rejected, and the remaining events can be classified as charged curent or neutral current, on an event-by-event basis. For the neutral current events, the hadron shower energy and angle can be calculated immediately. For each charged current event, the muon track is first eliminated to calculate the hadron shower energy and angle. This minimizes any bias in direct neutral current and charged current comparisons. The muon track is then restored to reconstruct the muon momentum for the usual charged current analysis. Pertinent reconstructed information for each event is then added to the event in a "Data Summary Tape(DST)" block. The PHYSICS program then uses the DST and any other information to analyze each event and derive physics results.

IV.1 Event Selection

To ensure the highest efficiency for event reconstruction, all events have been scanned by the staff of the Film Analysis Facility at Fermilab, and pattern recognition programs have been developed in parallel to

determine and minimize the systematic uncertainties.

A physicist scan of the events determined that the scanners rejected less than 1 % of neutrino events. The computer analysis program was required to reconstruct all events accepted by the scanners. The analysis of all events rejected by the scanners recovered few neutrino events. The physicist scan also determined that less than 1 % of the accepted events are due to cosmic rays.

IV.1.1 Fiducial Volume

To obtain a clean set of pion band events, we have set a very conservative fiducial volume in the analysis. Although the active area of the detector is 12′ by 12′, only events with vertex inside a one meter radius from the beam center are accepted.

Due to the beam geometry, and the decay kinematics, the neutrinos from ($K_{\mu 2}, K_{\mu 3}$, and K_{e3}) decays have average radii greater than the average radius for the neutrinos from the pion decay. At our distance from the decay pipe, and for the momentum settings selected, the average of the radial distrubution for neutrinos for each of the background decay modes is greater than 1.5 meters. Most of the neutrinos from the pion decay are contained within a 1 meter radius.

Neutrinos from decays before the momentum selection ("the Wide

Band Background") have an approximately uniform distribution in area. A reduction from 1.4 meter radial acceptance cut to 1.0 meter cut reduces this background by a factor of 2. This is particularly important for the −165 GeV/c momentum setting, where the desired incident particles are antineutrinos. The wide band background there is potentially large, because it contains neutrinos which have relatively high cross section.

This tight radial cut represents a small (depending on the momentum setting of the secondary particles) loss of the pion band events, while reducing a substantial fraction of the background events. A tight radial cut also decreases the inefficiency for identifying charged current events.

In addition, longitudinal cuts are imposed. The vertex of an event is required to be greater than 4 flash chambers (12 cm) from the front of the detector, to eliminate upstream interactions. Each accepted event is also required to have the vertex more than 208 flash chambers ($\simeq$ 630 cm, $\simeq$ 8 absorption lengths) from the back of the calorimeter, to ensure the containment of the hadron shower.

IV.1.2 Kinematic Cuts

To achieve good comparisons between the neutral current and the

charged current, two kinematic cuts are imposed on the data during the analysis.

The hadron shower energy E_{he} of each event is required to be greater than 10 GeV. This requirement ensures that the neutral current and the charged current have the same trigger and reconstruction efficiencies. It also reduces the small cosmic ray and wide band background, since they mostly produce low energy showers.

The second kinematic cut imposed on the data is that E_{he}/E_{ν} be less than 0.8, where E_{ν} is the mean energy of the pion band neutrinos obtained from the energy–radius correlation. This requirement eliminates the kinematic region in which the efficiency to classify the event correctly as neutral current or a charged current event is less than 98 %. Furthermore, it reduces the contamination from (K_{μ_2}, K_{μ_3}, and K_{e_3}) decays, since most of these events produce higher E_{he} showers. It is particularly helpful in eliminating nearly all of the K_{e_3} charged current events (since the total energy of the incident neutrino energy is measured) which would otherwise be misclassified as neutral current events.

The background and corrections after the above cuts will be discussed in Chapter VI.

In the present analysis, the absolute normalization of charged current or neutral current events is not required, since the results are based on the ratio of neutral current distributions to charged current distributions. It is important, however, to have the same acceptance and resolution for the neutral current and the charged current events, and correct for differences when neccessary. In addition to requiring the same kinematic reconstruction for the neutral current and the charged current events, a complete Monte Carlo program has been developed to study the effects of acceptance and resolution.

IV.2 Monte Carlo Simulation

The complete Monte Carlo program is composed of several components:

1. The neutrino beam simulation. This has been described in section II.5.

2. The four–vector event kinematics generation. The starting point of this program is the files of neutrinos created by the beam Monte Carlo. The kinematics of an event being simulated is determined from the energy of the neutrino, and the generated values of the scaling variables x and y. The probability for each event is determined by the

cross section weight evaluated using E_ν, x, and y, and assumed structure functions. A wide range of structure functions, from simple forms to more sophiscated fits that include QCD effects, have been used to study the sensitivity of our results to the structure functions assumed. The generated true values of the measurable quantities can be smeared using the resolution functions ($Eq.III.1 - Eq.III.4$).

All measurable quantities, true and/or smeared, can be written onto tapes to be analyzed by the same program that analyzes the data. Self consistency checks have shown that the analysis program gives the generated values on an event–by–event basis, and the generated distributions for all measureable quantities.

3. The complete shower generation. The shower generation[33] incorporates the properties and geometry of the detector, together with general characteristics of electromagnetic and hadronic showers. The critical energy and the radiation length are taken into account in the generation of electromagnetic showers. Existing data [34] on x–Feynman distributions, inclusive hadron–nucleon cross sections and multiplicity are incorporated in the hadron shower generation, together with the absorption length of the detector, efficiencies of the chambers, and the decay of the hadrons.

The reconstructed quantities for the generated showers have been compared with those quantities for the calibration hadron showers at the calibration beam energies. The quantities include : total number of hits, average density, average width, length, total proportional chamber pulse height, reconstructed energy, reconstructed angle and angular resolution. The comparisons are shown in Fig. IV.1.

In the energy range between 10 GeV and 50 GeV, $1.1 \pm .2\%$ of the calibration hadron showers are misclassified by the pattern recognition program as CC (charged current). On the average, $1.3 \pm .2\%$ of the calibration–hadron–like Monte Carlo generated showers in the same energy range are misclassified as CC. The charged current or neutral current event classification is discussed in the next section.

IV.3 CC or NC Classification

Fig. IV.2.a shows a typical neutral current event, while Fig. IV.2.b shows a charged current event. For any neutral current analysis, it is important that the highest efficiency be obtained for the separation of neutral current events from charged current events. To achieve this goal, we have required that :

1. all events have been scanned by the staff of the Film Analysis Facility at Fermilab.

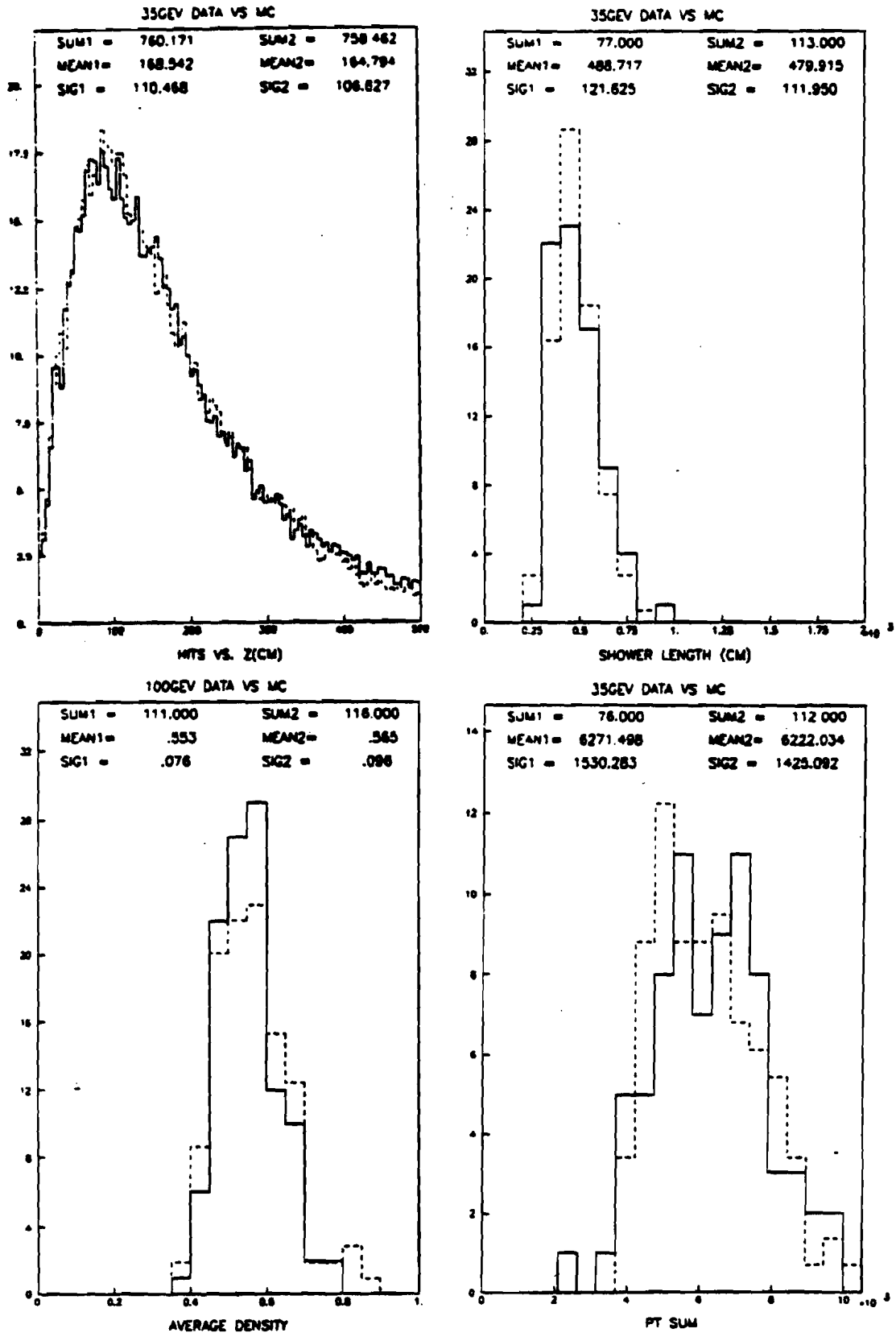

Fig. IV.1 Monte Carlo versus calibration

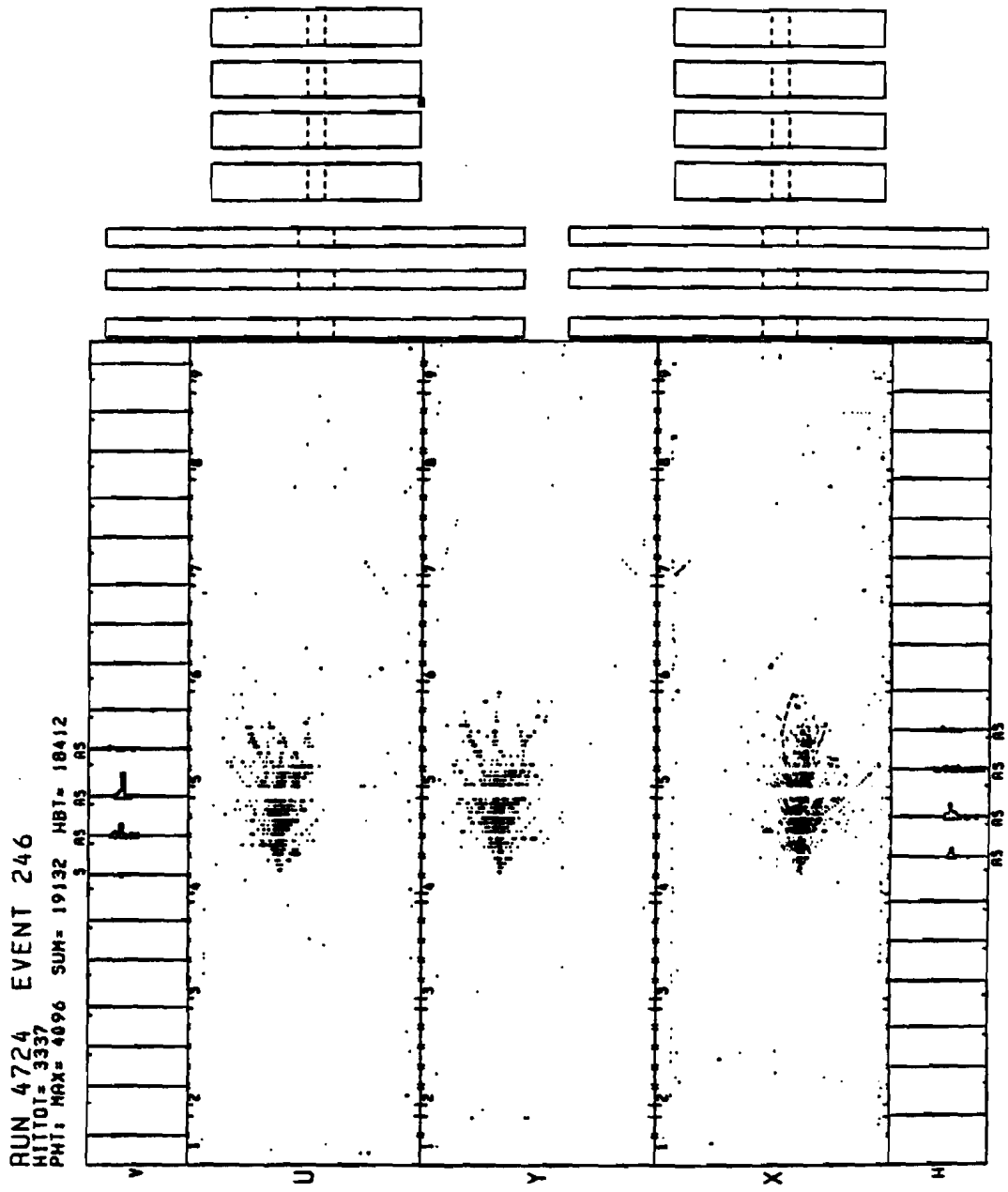

Fig. IV.2.a neutral current event

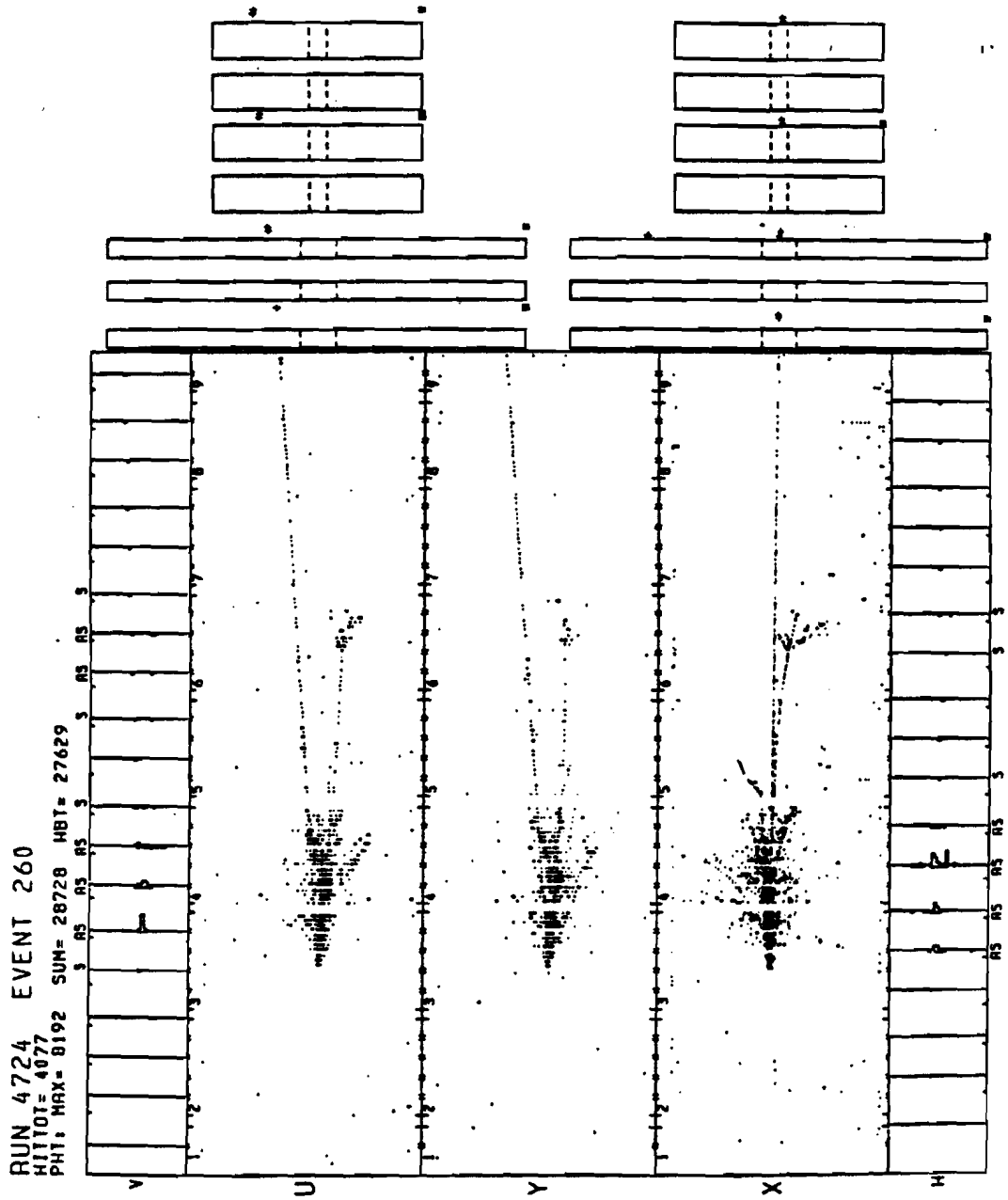

Fig. IV.2.b charged current event

2.a pattern recognition computer program is developed with the efficiency $\mathcal{E}_{CC}$ for identifying charged current events and the efficiency $\mathcal{E}_{NC}$ for identifying neutral current events, comparable to the efficiencies from scanning to minimize systematic uncertainties.

3. we use only the kinematic region for which the efficiencies $\mathcal{E}_{CC}$ and $\mathcal{E}_{NC}$ are nearly 100 %, since, physically, the analysis can be done over any kinematic range. (i.e. our physics goal does not require that we cover the entire physical kinematic range)

In the scanning, an event is classified as charged current if it had a track with length greater than 10 interaction lengths(500 cm), and with no apparent interaction in the detector. (A track is defined as a series of at least 3 flash chamber hits in any view that are in line with the vertex) Otherwise, it is classified as a neutral current event.

Over most of the kinematic region, the angle of the muon is less than 150 mrad, and the track is clearly visible in both the calorimeter and in the toroid chambers. With this scan rule, the scanning efficiency is greater than 99 % for identifying charged current events, as determined by scanning Monte Carlo generated events, over most of the kinematic region. In the region of $y \approx 1$, when the energy of the muon is below 2 GeV, the efficiency falls rapidly.

The computer algorithm is required to have the same efficiency for finding charged current events. The algorithm creates an angular histogram at the vertex, in the range $(+50, -50)$ degrees along the neutrino beam direction, with a 2 degree bin size, to find 2 muon track candidates in each view of the flash chambers. The track candidates are matched to find a charged current muon candidate.

As a check of the event classification, we analyzed both calibration hadron showers and charged current events with the muon eliminated. These events should not have charged current muon candidates. This allows us to determine the efficiency for the program to identify neutral current events to be greater than 98 %.

The event classification from visual scanning has been important in developing the pattern recognition program. To maximize consistency, the classification using the computer program is used in the analysis. The correction for the CC and NC misclassification is described in section VI.4.1.

IV.4 Kinematic Reconstruction

For the most direct comparisons between the neutral current and the charged current, it is crucial that the reconstructed neutral current and charged current events cover the same kinematic range and have the same resolutions to minimize biases. To achieve this goal, hits due to the CC muon are eliminated for these comparisons, and the kinematic variables of both the charged current events and the neutral current events have been reconstructed using the measured E_{he} and θ_{he}, together with E_ν from E_ν–radius correlation :

$$y = \frac{E_{he}}{E_\nu}$$

$$x = \frac{E_{he} \sin^2 \theta_{he}}{2M(cos^2\theta_{he} - y)}$$

V. Charged Current Analysis

The charged current events, for the purpose of the present analysis, provide good verifications of the kinematic reconstruction the neutral current analysis. These verifications are described in this chapter.

The energy–radius correlation of the incident neutrino from the analysis[31,32] of the quasi–elastic events in which the muon carries nearly 100 % of the incident neutrino energy is in good agreement with the beam Monte Carlo prediction (see Chapter II). The neutrino energy ($P_\mu + E_{he}$) distribution as a function of the radius for the charged current events is shown in Fig. V.1.

Hadron shower energy distributions of the charged current events for the four train momentum settings are shown in Fig. V.2 together with the Monte Carlo predictions. Similarly, the angular distributions are shown in Fig. V.3. In addition, the balance between the transverse momentum measured from the muon and the tranverse momentum measured from the hadron shower provides a consistency check of the energy and angle measurements. We believe that the energy and angle of the hadron showers are well measured, and the resolutions are understood.

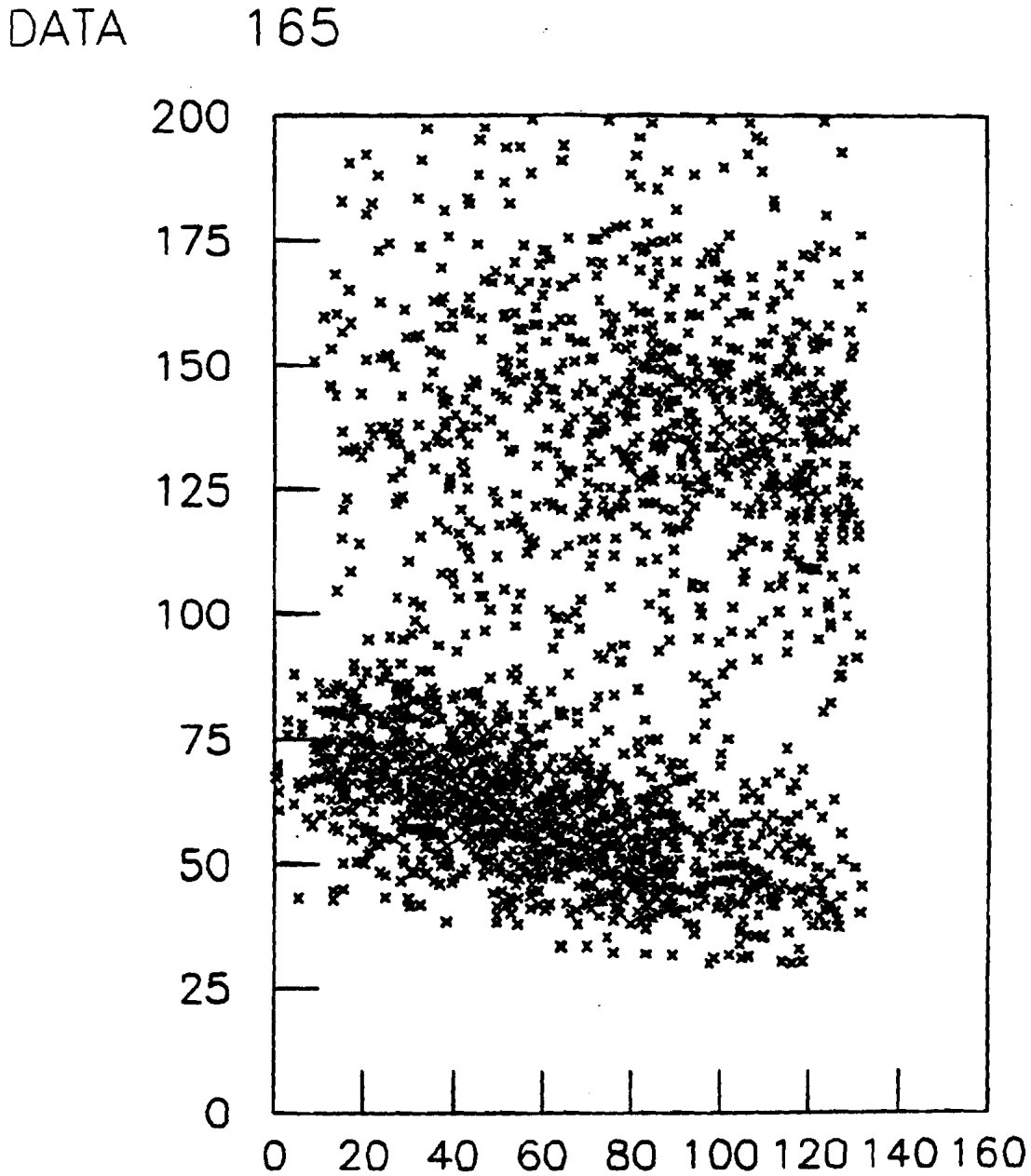

Fig. V.1 E_ν vs radius

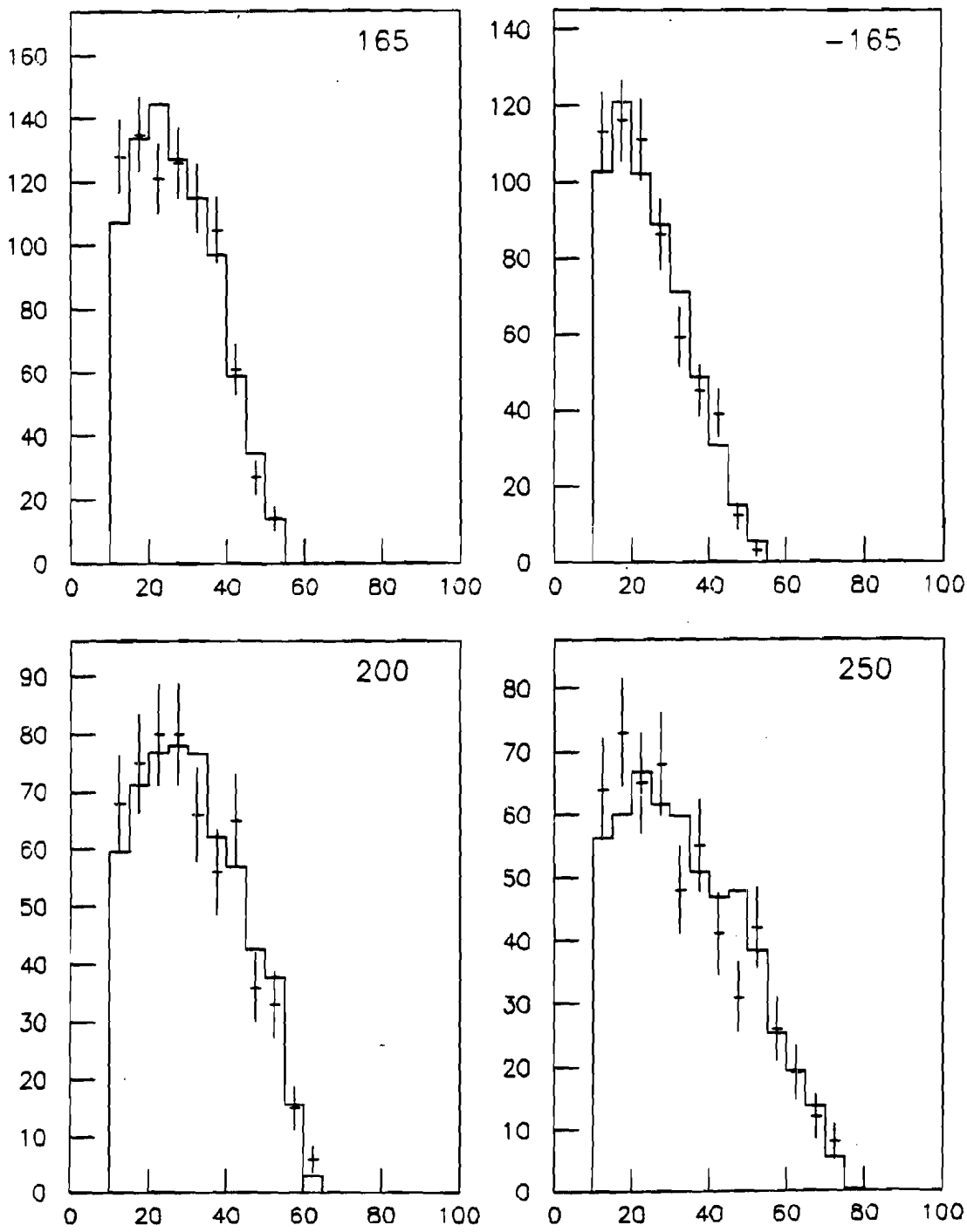

Fig. V.2 E_{he}

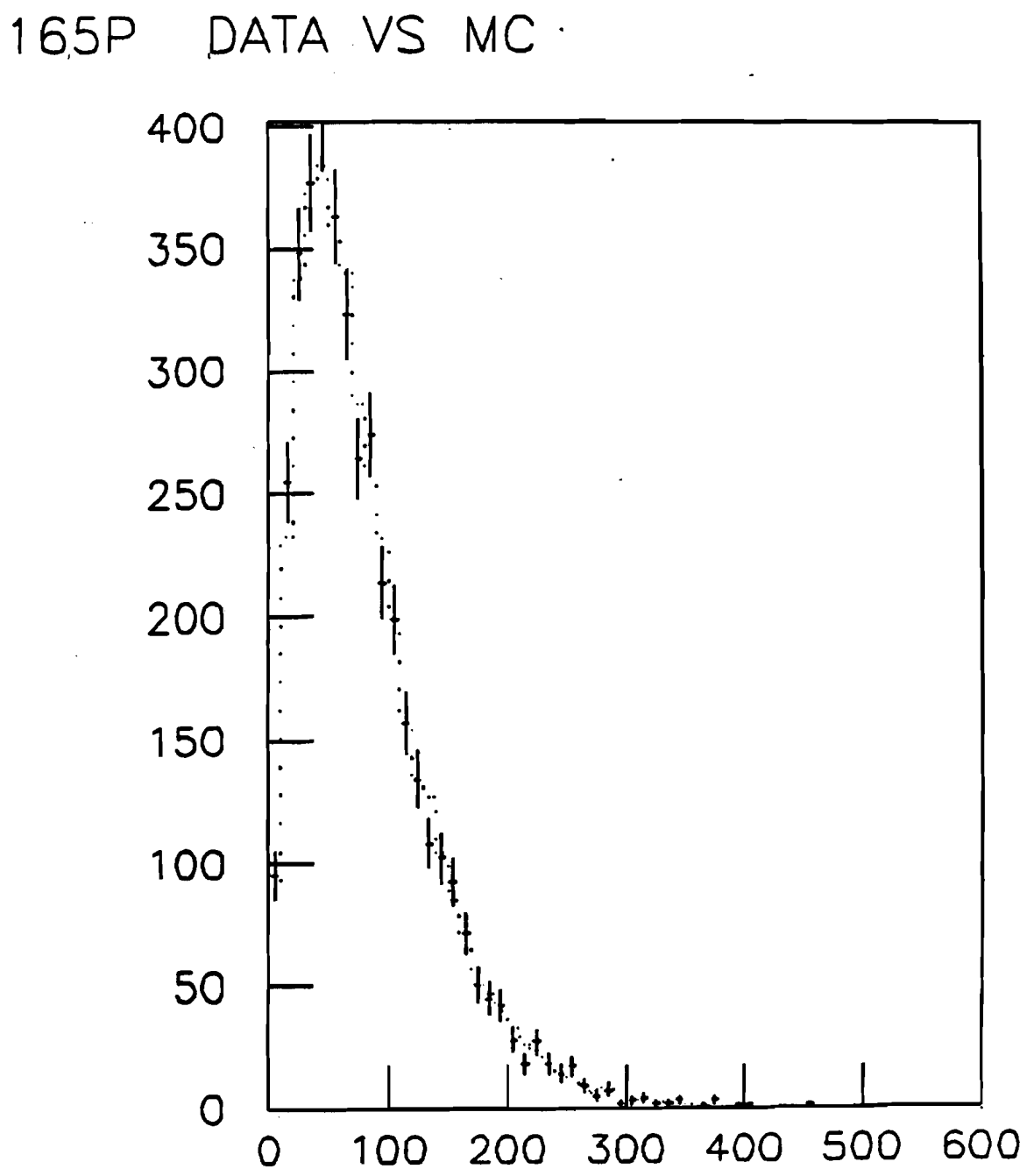

Fig. V.3 θ_H

Results of the standard charged current analysis, using information from the muon, are consistent with existing data[4,6], and are in good agreement with our Monte Carlo calculations. The results of the continuing analysis, incorporating absolute normalization to separate the structure functions $F_2^{CC}(x)$ and $xF_3^{CC}(x)$ (also $F_2^{NC}(x)$ and $xF_3^{NC}(x)$), will appear in future theses and publications.

VI. Neutral Current Analysis, with comparison to Charged Current

For direct comparisons, the charged current events (after the elimination of the muon track) have been analyzed with the same program that analyzes the neutral current events. Only events with hadron shower energy ($E_{hs} = E_H - M$) greater than 10 GeV are accepted. Thus, the trigger efficiency is $\simeq$ 100 % for both the neutral current and charged current events.

In the present analysis, we select events in which the incident neutrino has come from a pion decay to minimize systematic errors due to background and misclassification. Furthermore, we require y to be less than 0.8, and the event vertex to be inside a 1 meter radius from the beam center. With these constraints, the events with incident neutrino from 3-body kaon decays are less then 1 %, and less than 10 % from 2-body kaon decay. They are taken into account in the Monte Carlo calculations.

VI.1 The Distributions

We first compare the various distributions between the neutral current and the charged current events. The Q^2 distribution for the neutral current events is in good agreement with the Q^2 distribution for the charged current events. The Q^2 distributions, normalized to equal

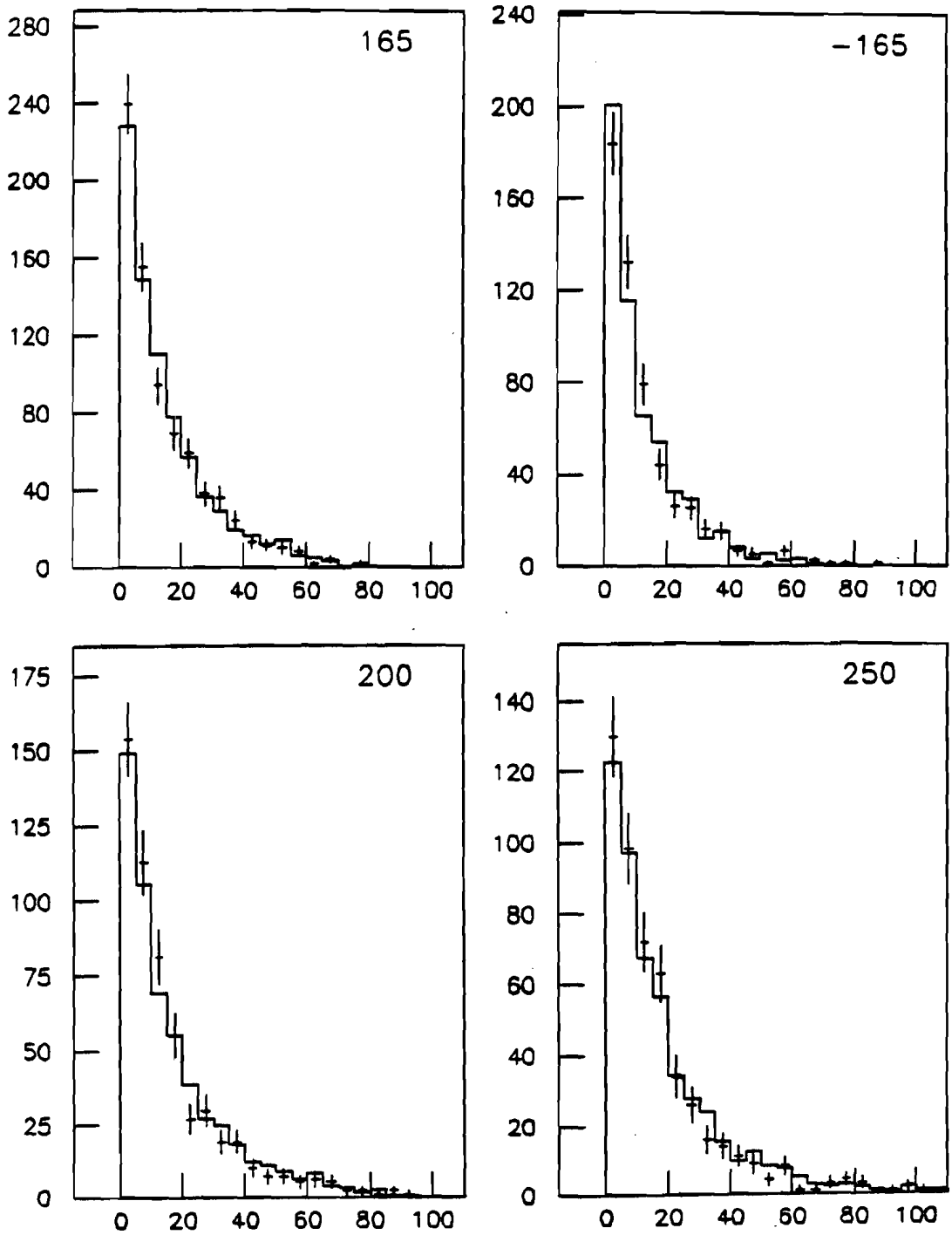

Fig. VI.1 NC and CC Q^2 distributions

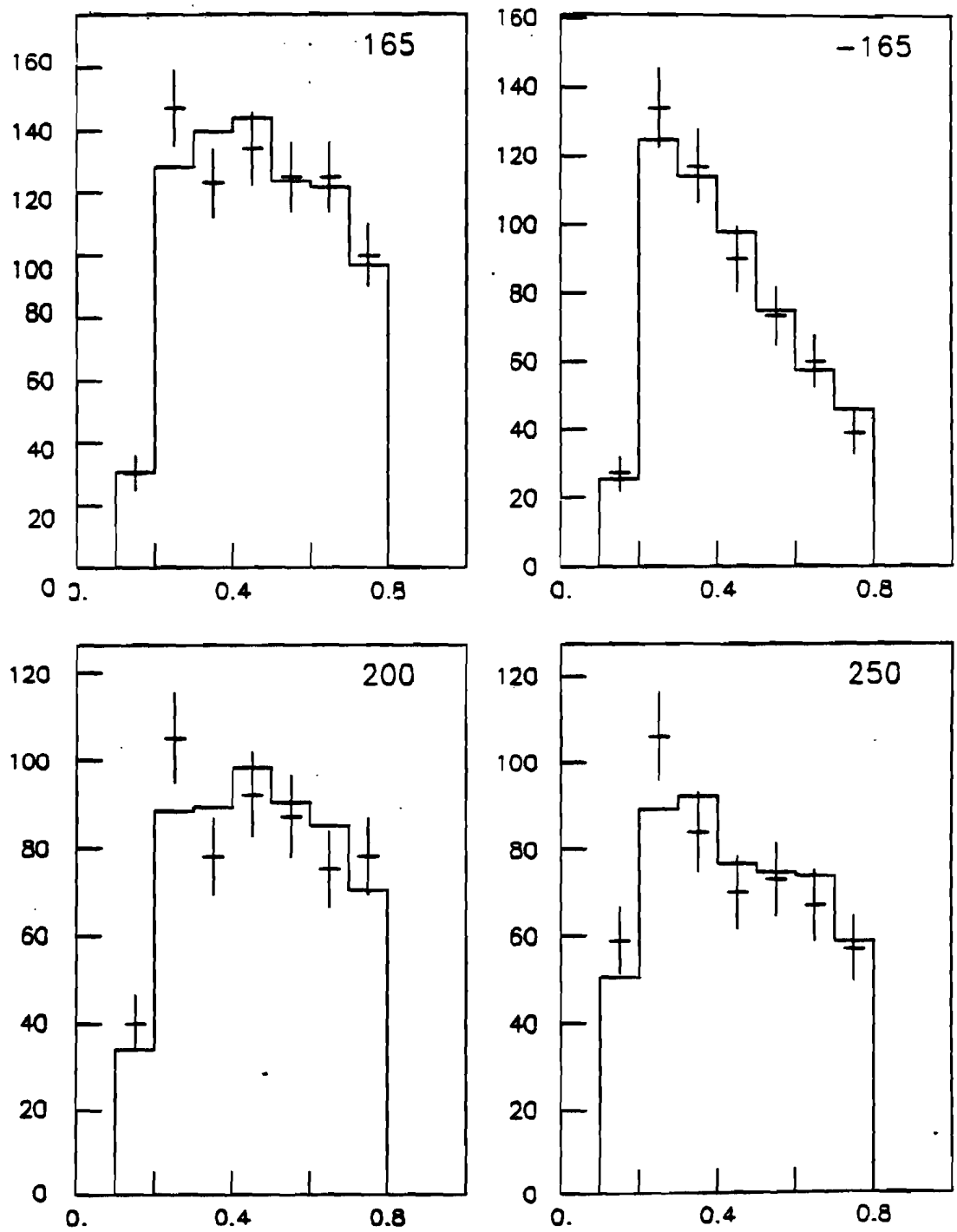

Fig. VI.2 NC and CC y distributions

total number of events (which is the number of neutral current events at each momentum setting) are shown in Fig. VI.1 for both neutrinos (train momentum setting at +165, +200, +250) and antineutrinos (train momentum setting at −165). Similarly, the y distributions are shown in Fig. VI.2. Good agreement between the shapes of the momentum x distribution for neutral current and for charged current is shown in Fig. VI.3.

These comparisons, between the distributions for the neutral current events and the distributions for the charged current events, are in good agreement with the Monte Carlo calculations. In the more rigorous analysis in the following section, we shall integrate over the accepted y region, and analyze only in terms of x distributions.

VI.2 The Ratio Tests

Fig. VI.4 shows the neutral current to charged current ratio of x distributions for the various secondary momentum beam settings of the narrow band beam. The predicted ratios from the Standard Model have essentially no x-dependence.

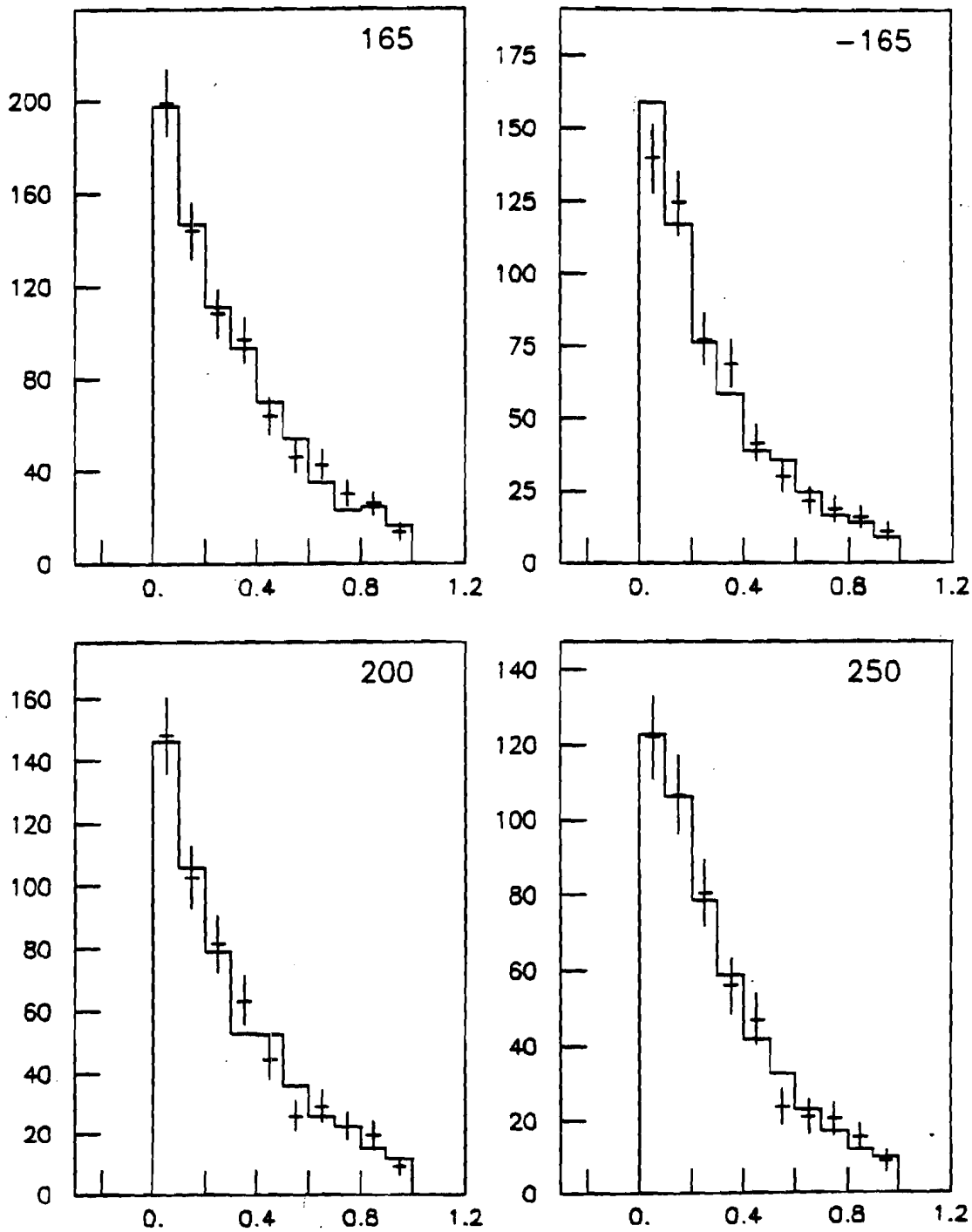

Fig. VI.3 NC and CC x distributions

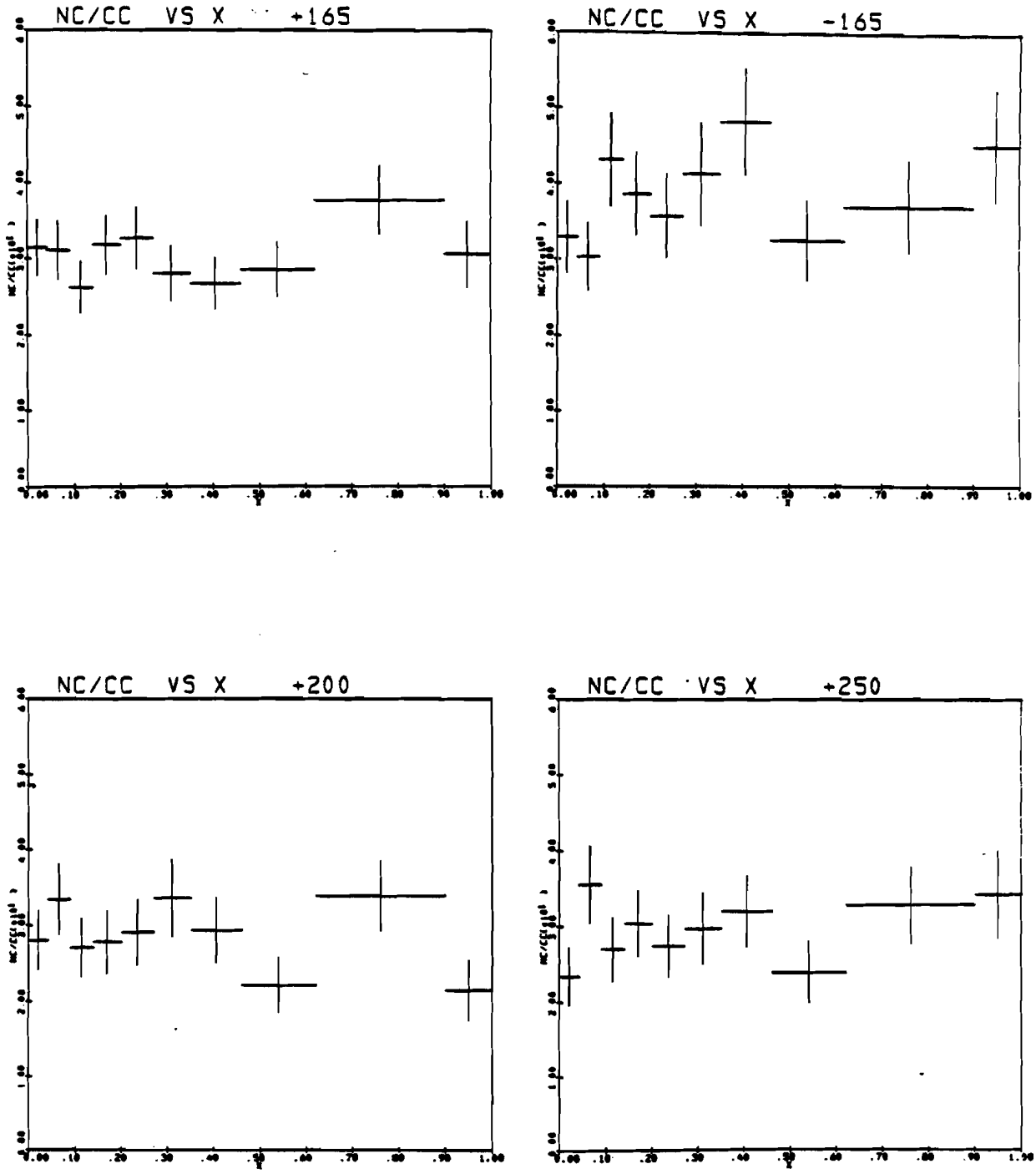

Fig. VI.4 Ratio of x distributions

More quantitatively, we make the following definition :

$$F_2^{NC}(x) = (\frac{1}{2} - \sin^2\theta_w + \frac{10}{9}\sin^4\theta_w)\tilde{F}_2^{NC}(x)$$
$$+ (d_L^2 + d_R^2 - u_L^2 - u_R^2)x[s(x) + \bar{s}(x) - c(x) - \bar{c}(x)] \qquad (VI.1)$$
$$xF_3^{NC}(x) = (\frac{1}{2} - \sin^2\theta_w)x\tilde{F}_3^{NC}(x)$$

Thus, $\tilde{F}_2^{NC}(x)$ and $x\tilde{F}_3^{NC}(x)$ have been defined to be the distributions $x[q(x) + \bar{q}(x)]$ and $x[q(x) - \bar{q}(x)]$ in Eq. I.30. $x\tilde{F}_3^{NC}(x)$ corresponds to the momentum distribution of the valence quarks, while $\tilde{F}_2^{NC}(x)$ corresponds to the momentum distribution of all quarks and antiquarks (valence + sea), as seen by the neutral current. We shall parametrize these functions as :

$$\tilde{F}_2^{NC}(x) = Ax^\alpha(1-x)^\beta + C(1-x)^\gamma$$
$$x\tilde{F}_3^{NC}(x) = Ax^\alpha(1-x)^\beta \qquad (VI.2.a)$$

For the form of the structure functions, the Drell–Yan–West relation[35] suggests that $(1-x)^3$ dominates at high x while Regge arguments[2] suggest a $\sqrt{x}$ dependence at low x. The $C(1-x)^\gamma$ term corresponds to the momentum distribution of the sea quarks. The charged current data[4] indicate a value of 6.5 ± .5 for γ, consistent with the value of 7 expected from counting rules.[36] For the purpose of comparison, we shall adopt the parametrization Eq. VI.2.a for the neutral current, and parametrize the charged current structure functions similarly as :

$$F_2^{CC}(x) = A_{CC}x^{\alpha_{CC}}(1-x)^{\beta_{CC}} + C_{CC}(1-x)^{\gamma_{CC}}$$
$$xF_3^{CC}(x) = A_{CC}x^{\alpha_{CC}}(1-x)^{\beta_{CC}} \qquad (VI.2.b)$$

The CERN program MINUIT[37] has been used to determine the values of the parameters $(A, \alpha, \beta, C, \gamma)$ by minimizing the quantity chi-squared defined as follows :

$$\chi^2 = \sum_j \frac{\left(\frac{n_j^{NC}(x)}{n_j^{CC}(x)} - \frac{N_j^{NC}(x)}{N_j^{CC}(x)}\right)^2}{\sigma_j^2} \qquad (VI.3)$$

where

$$N_j^{NC}(x) = \mathcal{N} \int \frac{dn_\nu}{dE_\nu} E_\nu \, dE_\nu \left[\left(\int \epsilon(x,y)(1 - y + \frac{y^2}{2}) \, dy \right) F_2^{NC}(x) \pm \left(\int \epsilon(x,y)(y - \frac{y^2}{2}) \, dy \right) x F_3^{NC}(x) \right] \qquad (VI.4.a)$$

$$N_j^{CC}(x) = \mathcal{N} \int \frac{dn_\nu}{dE_\nu} E_\nu \, dE_\nu \left[\left(\int \epsilon(x,y)(1 - y + \frac{y^2}{2}) \, dy \right) F_2^{CC}(x) \pm \left(\int \epsilon(x,y)(y - \frac{y^2}{2}) \, dy \right) x F_3^{CC}(x) \right] \qquad (VI.4.b)$$

$N_j^{NC}(x)$ is the number of events in jth x bin of the neutral current x–distribution. $\epsilon(x,y)$ is the acceptance and smearing factor. Similarly, $N_j^{CC}(x)$ is the number of events in jth x bin of the charged current x–distribution. The normalization factor $\mathcal{N}$ and the flux factor

$$\int \frac{dn_\nu}{dE_\nu} E_\nu \, dE_\nu$$

are the same for neutral current and for charged current, and cancel in the ratio. $n_j^{NC}(x)$ is the predicted number of events in the jth x bin

of the neutral current x–distribution. Similarly, $n_j^{CC}(x)$ is the predicted number of events in the jth x bin of the charged current x–distribution.

The fitting procedure uses the Monte Carlo method for predicting the number of events in each bin, based on 100000 tries each for neutral current and charged current. A set of values of the parameters $(A_{CC}, \alpha_{CC}, \beta_{CC}, C_{CC}, \gamma_{CC})$ which is in agreement with a simple fit to the existing charged current data has been used for the charged current. (These values have been varied within their errors. The difference between these values for the charged current and the best fit values for the neutral current is insensitive to the exact values used for the charged current)

The prediction uses the same equal statistics bins as the data. The x bins used are :

$$0., 0.041, 0.089, 0.14, 0.20, 0.27, 0.35, 0.46, 0.62, 0.90$$

The last bin includes all events with x above 0.90, and takes into account the tail of the distribution due to smearing.

In each iteration of the MINUIT fit, a new set of values of the parameters $(A, \alpha, \beta, C, \gamma)$ for the neutral current structure functions is selected to seek the minimum χ^2 value of Eq. VI.3. The program calculates the Monte Carlo prediction, based on the current set of values of

the parameters, for the number of events in each bin taking into account the effects of acceptance and smearing. Eq. VI.3 is then evaluated for the χ^2 for the current iteration.

To check the fitting procedure, files of simulated neutrino events have been generated with different neutral current structure functions assumed for different files. The analysis method correctly determines the neutral current structure functions assumed for each file to within expected uncertainties.

For the purpose of comparison between the neutral current and the charged current, we use the following values for the charged current parameters which are consistent with their experimentally determined values :

$$\begin{aligned} \alpha_{CC} &= 0.5 \qquad A_{CC} = 3.3 \\ \beta_{CC} &= 3. \qquad C_{CC} = 1. \\ \gamma_{CC} &= 7. \end{aligned} \tag{VI.5}$$

From the data, the following results have been obtained:

Assuming $\alpha = \alpha_{CC}$ and $\gamma = \gamma_{CC}$ then :

$$\begin{aligned} A &= 3.14 \pm .62 \\ \beta &= 3.08 \pm .35 \\ C &= 1.04 \pm .21 \end{aligned} \tag{VI.6}$$

Assuming $A = A_{CC}$ and $\gamma = \gamma_{CC}$ then :

$$\begin{aligned} \alpha &= 0.52 \pm .07 \\ \beta &= 2.94 \pm .17 \\ C &= 1.02 \pm .22 \end{aligned} \tag{VI.7}$$

The existing data on neutral current structure functions are from two collaborations. The first published data from the bubble chamber group[18] was based on 23 neutral current events from a relatively low energy experiment, with an average E_ν of 12 GeV. The result from a subsequent run, based on 151 events, has been been published[20] recently. The CHARM Collaboration[19] has analyzed their data based on 1967 neutrino and 863 antineutrino neutral current events with $E_{h\nu}$ greater than 4 GeV. In their analysis, events are analyzed statistically : each event is assigned a certain probability of having $E_\nu = E_\nu^\pi$ or E_ν^k. The neutral current x distributions, with absolute normalization, are then unfolded for resolution and acceptance to obtain the parameters of the neutral current structure functions. The charged currents have also been analyzed using the same method for comparison. The results from the CHARM experiment are shown in Table VI.1 and Fig. VI.5.

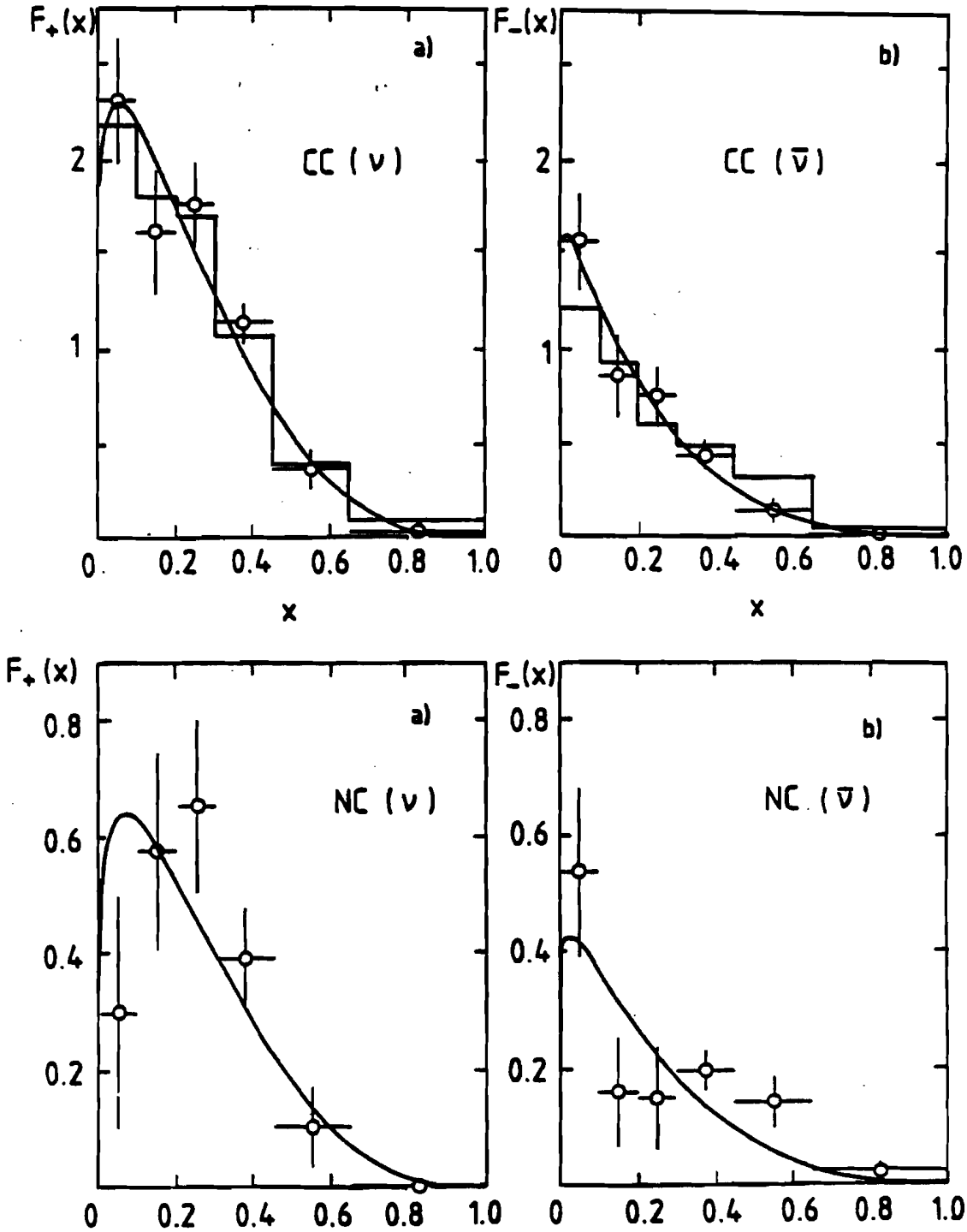

Fig. VI.5 x distributions from CHARM Collaboration

$$F_+^{CC}(x) = 2q_{val}(x) + \frac{8}{3} q_{sea}(x)$$

$$F_-^{CC}(x) = \frac{2}{3} q_{val}(x) + \frac{8}{3} q_{sea}(x) ,$$

using the parametrizations

$$q_{val}(x) = \frac{3}{\beta(a,\ b+1)} x^a(1-x)^b$$

$$q_{sea}(x) = C(c+1)(1-x)^c .$$

$\beta(a,\ b+1)$ is Euler's beta function used for normalization, assuming $\int(q_{val}/x)\ dx = 3$,

(1)	(2)	(3)	(4)	(5)
Parameter	CC with muon measurement	CC from unfolding	NC from unfolding	Systematic errors
a	0.47 ± 0.02	0.45 ± 0.05	0.44 ± 0.05	±0.05
b	2.71 ± 0.11	2.97 ± 0.16	2.79 ± 0.24	±0.09
$\bar{q}/(q+\bar{q})$	0.14 ± 0.005	0.17 ± 0.03	0.13 ± 0.03	±0.02

Table. VI.1 results from CHARM Collaboration

VI.3 $\sin^2\theta_w$

In the Standard Model,

$$\tilde{F}_2^{NC}(x) = F_2^{CC}(x) \qquad (VI.8)$$

and the only free parameter is $\sin^2\theta_w$. By setting the values of the parameters $A, \alpha, \beta, C, \gamma$ to be the same for $\tilde{F}_2^{NC}(x)$ and $F_2^{CC}(x)$ in Eq. VI.1, the value is determined to be :

$$\sin^2\theta_w = 0.243 \pm 0.013 \qquad (VI.9)$$

The uncertainty above is statistical. We estimate an additional systematic uncertainty of 0.01 due to CC or NC classification. Electroweak radiative correction, estimated to be about −.01, has not been appled to this result.

In the Standard Model, all neutral current coupling may be expressed in terms of $\sin^2\theta_w$, thus precise measurements of the value of $\sin^2\theta_w$ in different processes provide valuable tests of the Model. We summarize the results of some relatively high precision measurements.

1. recent results from proton–antiproton collisions :

Expt.	M_W	M_Z	$\sin^2\theta_w(M_W)$
$UA1^{(15)}$	$80.9 \pm 1.5 \pm 2.4$	---	$0.226 \pm .008 \pm .014$
$UA1^{(15)}$	---	$95.6 \pm 1.4 \pm 2.9$	---
$UA2^{(16)}$	$81.0 \pm 2.5 \pm 1.3$	---	$0.226 \pm .014 \pm .007$
$UA2^{(16)}$	---	$91.9 \pm 1.3 \pm 1.4$	$0.227 \pm .009 \pm .010$

These values of $\sin^2\theta_w$ were obtained from the mass of the W or the Z^0 boson, and included electroweak radiative corrections.

2. from Z^0–γ interference in deep inelastic scattering :

$$SLAC - YALE^{(12)} \quad \sin^2\theta_w = 0.220 \pm 0.012 \pm 0.008$$

The radiative correction[38] to be added to this value from the experiment is about –.01.

3. from recent high statistics neutrino experiments[14] :

Expt.	R_ν	$R_{\bar\nu}$	$\sin^2\theta_w$
CDHS	$.307 \pm .008$	$.373 \pm .025$	$0.230 \pm .013$
CHARM	$.320 \pm .010$	$.377 \pm .020$	$0.220 \pm .014$

In these values, the statictical and the systematic errors have been combined in quadrature, but the electroweak radiative corrections (estimated to be about –.01[38]) have not been applied. Since their publication, these values have influenced strongly the average value of $\sin^2\theta_w$ from all deep inclastic neutrino scattering experiments due to the relatively small quoted errors. These values have frequently been compared with the predictitions of $\sin^2\theta_w$ based on the $SU(5)$ theory.

The CDHS Collaboration has completed their analysis recently and has the new results :

$$CDHS(83) \quad R_\nu = .300 \pm .005 \pm .005$$
$$R_{\bar{\nu}} = .357 \pm .0095 \pm .0115$$
$$\sin^2\theta_w(20GeV^2) = .232 \pm .012$$

This new value of $\sin^2\theta_w$ includes the radiative correction. Statictical and systematic errors, which are equal, have been combined in quadrature.

The following result, which does not include radiative corrections, has been obtained recently by the $CFRR$ Collaboration :

$$CFRR \quad \sin^2\theta_w = .248 \pm .012 \pm .015$$

VI.4 Background and Corrections :

In the analysis, we have adopted the philosophy of minimizing the sensitivity of results to systematic uncertainties. The method, using $R(x, y)$, enables us to make the comparisons between the neutral curent and the charged current interactions in any finite kinematic region. The results have been obtained from the (x, y) regions in which the background and corrections are a few percent for neutral current or charged current events. Furthermore, the remaining uncertainties approximately cancel in the ratio, and the results are insensitive to these uncertainties.

VI.4.1 CC and NC misidentification

The charged current and neutral current event classification is potentially a source of large systematic errors in any neutral current analysis. The dominant difficulty in classification is identifying the low energy muon for charged current events with high y. The effect due to this difficulty is substantially reduced by excluding events with y greater than 0.8 for the analysis.

To determine the percentage inefficiency in classifying charged current events, δ_{cc}, and the inefficiency in classifying neutral current events, δ_{nc}, we have generated and analyzed 40000 Monte Carlo events at each train momentum setting, in addition to carrying out the studies described

in section IV.3. The CC inefficiency δ_{cc} is thus determined to be 2 % for the pattern recognition program, and the NC inefficiency δ_{nc} is also 2 % over the entire range of y . Approximately half of the CC events misclassified as NC have reconstructed x less than 0.1. The NC events misclassified as CC have little kinematic dependence. This x dependent small correction due to CC and NC misidentification has been made in the final analysis.

VI.4.2 Muon Bremsstrahlung

The probability for the muon to bremsstrahlung, producing a photon with energy in excess of 1 GeV in the calorimeter is 1%. This is reduced by a factor of 4 for the photon to be inside and considered as part of the hadron shower, since the average shower length is one fourth the length of the calorimeter. Thus, the effect due to muon bremsstrahlung is negligible.

VI.4.3 Radiative Correction

The probability for a muon of energy $\tilde{E}_\mu$ to radiate a photon of energy k at the vertex can be expressed as[39] :

$$\frac{dP}{dk} = Nv\left(\frac{k}{\tilde{E}_\mu}\right)^v \frac{1}{k}\left[1-\left(\frac{k}{\tilde{E}_\mu}\right)+\frac{1}{2}\left(\frac{k}{\tilde{E}_\mu}\right)^2\right]$$

$$v = \frac{\alpha}{\pi} \ln \left[\frac{s(1-y+xy)^2}{\mu^2} \right]$$

The effective radiation length v is calculated to be 0.018 for the data. The corresponding average energy loss by the muon is 0.64GeV.

The effect of this "Internal Bremsstrahlung" is to deposit excess flash chamber hits along the direction of the muon. This is taken into account, and corrected on the average, when the muon track is eliminated for the energy and shower angle calculations.

VI.4.4 Resolutions

The sensitivity of the results, to experimental resolutions, has been studied. Any 10 % change in the E_ν, E_{he}, or θ_{he} scale would not affect the results. A 20 % increase in E_{he} resolution also would not affect the results, while a 20 % increase in θ_{he} resolution would increase the errors by 20 %.

The difference between the values of the parameters for the neutral current structure functions and the values for the charged current are insensitive to the precise fit values of the parameters for the existing charged current structure function data. This is clearly shown in the following table.

	$\Delta\beta = \beta - \beta_{CC}$	$\Delta C = C - C_{CC}$	
β_{CC}	$C_{CC} = 0.8$	$C_{CC} = 1.0$	$C_{CC} = 1.2$
2.8	$\Delta\beta = .04 \pm .10$	$\Delta\beta = .04 \pm .11$	$\Delta\beta = .05 \pm .11$
	$\Delta C = .03 \pm .11$	$\Delta C = .03 \pm .10$	$\Delta C = .04 \pm .10$
3.0	$\Delta\beta = .05 \pm .11$	$\Delta\beta = .05 \pm .12$	$\Delta\beta = .06 \pm .12$
	$\Delta C = .03 \pm .11$	$\Delta C = .04 \pm .11$	$\Delta C = .04 \pm .11$
3.2	$\Delta\beta = .05 \pm .11$	$\Delta\beta = .06 \pm .12$	$\Delta\beta = .07 \pm .12$
	$\Delta C = .05 \pm .12$	$\Delta C = .06 \pm .12$	$\Delta C = .06 \pm .12$

VI.4.5 K band contamination

In the NC and CC analyses without the energy of the outgoing lepton, it is not possible to determine with 100 % certainty whether the incident neutrino came from a pion decay or a kaon decay. From simple two-body decay kinematics, the energy E_ν^π of a neutrino from the decay of a pion with momentum P_0 is constrained by :

$$0 \leq \frac{E_\nu^\pi}{P_0} \leq 1 - \frac{m_\mu^2}{m_\pi^2}$$

In an analysis using the kaon band, the pion band events can be eliminated by imposing a minimum E_{h_e} cut, or equivalently, a minimum y cut. However, the cut would mean a loss of about half of the kaon neutrinos. Furthermore, the electron–type neutrino (from K_{e3} decay)

charged current events would be classified as neutral current. This is a large background that is difficult to eliminate in a K band analysis.

In the present analysis, which uses neutrinos from the pion band, the contamination of neutrinos from kaon decays is reduced by the requirements that the measured y be less than 0.8, and that the vertex be within 1 meter radius from the center of the neutrino beam. The remaining contamination is shown in Table VI.3.

P_0	$K_{\mu 2}$	$K_{\mu 3}$	K_{e3}	*Wide band*
GeV/c	%	%	%	%
+165	$7.2 \pm .3$	$.4 \pm .1$	$.7 \pm .2$	$.9 \pm .1$
+200	$9.6 \pm .2$	$.5 \pm .1$	$.7 \pm .2$	$.9 \pm .1$
+250	$12.5 \pm .2$	$.7 \pm .1$	$1.6 \pm .2$	$1.3 \pm .1$
−165	$6.0 \pm .4$	$.1 \pm .1$	$.3 \pm .1$	$1.3 \pm .1$

Contaminations from $K_{\mu 3}$, *or* K_{e3} decays are negligible, however, they are included together with the $K_{\mu 3}$ background in the Monte Carlo calculations, and in the MINUIT fit.

VI.4.6 Wide Band Background

The contamination of neutrinos from the decays of the secondary particles before the momentum selection, can be determined by closing

the collimator in the momentum selecting train. The accepted number of events, using the standard cuts for the analysis, normalized to the number of protons–on–target, determines the magnitude of this background. The wide band background has been determined to be less than 2 % for the neutrino data, and less than 2 % for the antineutrino data. This background is included in all Monte Carlo calculations, and in the MINUIT fit.

VI.4.7 Neutron Excess

The cross sections and the structure functions (Eq. I.23, Eq. I.30) have been calculated for isoscalar targets like deuterium. In the iron target planes, there are more neutrons than protons. In the flash chamber polyproplyene, there are more protons than neutrons.

For a target with N neutrons and Z protons, the correction to the isoscalar cross section for the charged current neutrino interactions is :

$$\frac{N-Z}{N+Z}\frac{G^2ME}{\pi}x\left(u(x)-d(x)\ -\ [\overline{u}(x)-\overline{d}(x)](1-y)^2\right)$$

and the correction for antineutrino interactions is :

$$\frac{N-Z}{N+Z}\frac{G^2ME}{\pi}x\left(\overline{u}(x)-\overline{d}(x)\ -\ [u(x)-d(x)](1-y)^2\right)$$

The neutron excess corrections for the neutral current cross sections are a factor of $\frac{1}{3}\sin^2\theta_w$ smaller.

Since the average $(N-Z)/(N+Z)$ of the calorimeter is $\simeq 2\ \%$, these corrections are negligible.

VI.4.8 Fermi Motion

In the calculations described in Chapter I, it has been assumed that the nucleon is at rest. Nucleons in all elements except hydrogen are not at rest in the laboratory system, due to nuclear binding effects. The effects due to the Fermi Motion are that the measured cross sections and structure functions differ from the values for nucleons at rest by $\approx$ 5 % over nearly all of the accessible region.[40]

The Fermi Motion corrections are the same for the neutral current and the charged current. They cancel in the ratio, and our comparisons between the neutral current structure functions and the charged current structure functions are independent of this correction.

VI.4.9 $s(x) - c(x)$

From the comparison between Eq. I.23 and Eq. I.24, it is clear that the charged current structure functions for the neutrino and the antineutrino scattering processes are slightly different from each other and from the experimentally measured structure functions $F_2^{CC}(x)$ and $xF_3^{CC}(x)$. Similarly, Eq. I.30 shows that the neutral current F_2 also

contains a term proportional to the difference between the strange and the charm quarks. (The value of this term in Eq. I.30 is positive)

In estimating these differences, it has been assumed that $s(x) = \bar{s}(x)$, and $c(x) = \bar{c}(x) \simeq 0$. In addition, the following result[41] is adopted,

$$\frac{2s(x)}{[\bar{u}(x) + \bar{d}(x)]} \simeq 0.5$$

The analysis has been done with and without taking these differences into account. Our results are insensitive to these differences.

VI.4.10 EMC effect

The recent discovery of the "EMC effect"[42] — that the momentum distribution of the quarks inside a nucleus is different from the momentum distribution of the quarks inside a free nucleon—has had a number of theoretical explanations.[43]

Our results determine the differences between the neutral current and the charged current structure functions, for the same target, and are insensitive to the absolute determination of the charged current structure functions from our target–calorimeter.

The charged current structure functions have been varied in the fits, the neutral current structure functions determined vary accordingly, however the differences (and the uncertainties) between the neutral cur-

rent and the charged current structure functions remain essentially unchanged.

VII. Conclusions

A direct comparison has been made between the momentum x distribution of the constituents inside a nucleon as probed by the neutral current, and the distribution as probed by the charged current. The data, obtained with the Lab C neutrino detector at Fermilab, provide a flux independent study that is the least sensitive to systematic uncertainties. The distributions are in good agreement, as predicted by the standard theory of electromagnetic and weak interactions together with the quark–parton model. We conclude that the weak neutral current sees the same constituents inside the nucleon as does the weak charged current.

In the context of the Standard Model, we have determined the value of the free parameter $\sin^2 \theta_W$, which is in good agreement the average value determined by previous experiments.

References

(1) E. D. Bloom, et al., Phys. Rev. Lett. 23 (1969) 930.

M. Breidenbach, et al., Phys. Rev. Lett. 23 (1969) 935.

G. Miller, et al., Phys. Rev. D5 (1972) 528.

J. S. Poucher, et al., Phys. Rev. Lett. 32 (1974) 118.

S. Stein, et al., Phys. Rev. D12 (1975) 1884.

A. Bodek, et al., Phys. Rev. D20 (1979) 1471.

(2) J. Kuti and V. F. Weisskopf, Phys. Rev. D4 (1971) 3418.

(3) R. P. Feynman, Proceedings of the Third International Conference on High energy Collisions, Stony Brook (1969)

R. P. Feynman, Photon-Hadron Interactions, W. A. Benjamin, INC. Reading, Mass. (1972).

(4) J.G.H. De Groot, et al., Z. Physik C 1 (1979) 143.

(5) S. M. Heagy, et al., Phys. Rev. D23 (1981) 1045.

P. C. Bosetti, et al., Nucl. Phys. B142 (1978) 1.

J. Morfin, et al., Phys. Lett. 104B (1981) 235.

H. Weerts, Ph.D. thesis, Aachen.

M. Jonker, et al., Phys. Lett. 109B (1982) 133.

F. Bergsma, et al., Phys. Lett. 123B (1983) 269.

(6) H. Abramowicz, et al., Z. Physik C 17 (1983) 283.

D. MacFarlane, et al., Fermilab–Pub–83/108–EXP (1983).

(7) J. J. Aubert, et al., Phys. Lett. 123B (1983) 275;

Phys. Lett. 105B (1981) 315; Phys. Lett. 105B (1981) 322.

A. R. Clark, et al., Phys. Rev. Lett. 51 (1983) 1826.

(8) H. D. Politzer, Phys. Rev. Lett. 30 (1973) 1346;

Physics Reports 14C (1974) 129.

D. Gross and F. Wilczek, Phys. Rev. Lett. 30 (1973) 1343;

Phys. Rev. D8 (1973) 3633; Phys. Rev. D9 (1974) 980.

(9) S. L. Glashow, Nucl. Phys. 22 (1961) 579.

S. Weinberg, Phys. Rev. Lett. 19 (1967) 1264.

A. Salam, Proceeding of 8th Nobel Symposium (ed. N. Svartholm).

Almquist and Wiksell, Stockholm, 1969. P. 367.

S. L. Glashow, J. Iliopoulos, and L. Maiani, Phys. Rev. D2

(1970) 1285.

(10) F. J. Hasert, et al., Phys. Lett. 46B (1973) 121.

(11) J. Bleitschau, et al., Phys. Lett. 73B (1978) 232.

P. Alibran, et al., Phys. Lett. 74B (1978) 422.

N. Armenise, et al., Phys. Lett. 86B (1979) 225.

H. Faissner, et al., Phys. Rev. Lett. 41 (1978) 213.

A. M. Cnops, et al., Phys. Rev. Lett. 41 (1978) 357.

L. A. Ahrens, et al., Phys. Rev. Lett. 51 (1983) 1514.

R. Heisterberg, et al., Phys. Rev. Lett. 44 (1980) 635.

F. Bergsma, et al., Phys. Lett. 117B (1982) 272.

J. Bleitschau, et al., Nucl. Phys. 114B (1976) 189.

N. Armenise, et al., Phys. Lett. 81B (1979) 385.

M. Jonker, et al., Phys. Lett. 105B (1981) 242.

(12) C. Y. Prescott, et al., Phys. Lett. 77B (1978) 347;

Phys. Lett. 84B (1979) 524.

A. Argento, et al., Phys. Lett. 120B (1983) 245;

(13) see e.g. the review by

B. Naroska, Proc. Lepton–Photon Symposium, Cornell, 1983.

(14) M. Holder, et al., Phys. Lett. 71B (1977) 222.

M. Jonker, et al., Phys. Lett. 99B (1981) 265.

C. Geweniger, et al., Proc. Int. Conf. Neutrino '79.

M. Deden, et al., Nucl. Phys. B149 (1979) 1.

F. Merritt, et al., Phys. Rev. D17 (1978) 2199.

P. Wanderer, et al., Phys. Rev. D17 (1978) 1679.

C. Geweniger, et al., Proc. Europhysics study Conf. on Electroweak Effects at High Energy, Erice (1982); Proc. Europhysics Conf. on High Energy Physics, Brighton (1983).

R. E. Blair, et al., Fermilab–Conf–83/76–EXP (1983).

(15) G. Arnison, et al., Phys. Lett. 122B (1983) 103;
Phys. Lett. 129B (1983) 273; Phys. Lett. 134B (1984) 469;
Phys. Lett. 126B (1983) 398.

(16) M. Banner, et al., Phys. Lett. 122B (1983) 476;
Phys. Lett. 129B (1983) 130.

(17) M. Jonker, et al., Phys. Lett. 102B (1981) 67.

(18) C. Baltay, et al., Phys. Rev. Lett. 44 (1980) 916.

(19) M. Jonker, et al., Phys. Lett. 128B (1983) 117.

(20) C. Baltay, et al., Phys. Rev. Lett. 52 (1984) 1948.

(21) J. D. Bjorken, Phys. Rev. 163 (1967) 1767;
Phys. Rev. 179 (1969) 1547.

(22) L. N. Hand, Ph.D. Thesis, Stanford Univ.(1961);
Phys. Rev. 129 (1963) 1834.

(23) C. C. Callan and D. J. Gross, Phys. Rev. Lett. 22 (1969) 156.

(24) M. Gell-Mann, Phys. Lett. 8 (1964) 214,
G. Zweig, CERN-preprints TH401, TH412 (1964).

(25) see e.g., C. Quigg, Gauge Theory of the Strong, Weak and
Electromagnetic Interactions, Reading, Mass.,(1983)

(26) T. F. Eldridge, Ph.D. thesis, MIT.

A. Bodek, et al, Z. Phys. C 18, (1983) 289.

R. Blair, et al., Fermilab–Pub– 83/26–Exp.

(27) D. Owen, private communication.

(28) F. E. Taylor, et al., Proc. of the IEEE Trans. on Nucl. Sci., VOL. NS-27 (1980) 30.

D. Bogert, et al., Proc. of the IEEE Trans. on Nucl. Sci., VOL. NS-29, NO. 1, (1982).

(29) T. F. Droege, et al.,IEEE NS–25, No. 1, Fdb. 1978.

(30) J. Bofill, et al., Proc. of the IEEE Trans. on Nucl. Sci., VOL. NS-29, NO. 1, (1982) 400.

(31) A. Cohen, Ph.D. thesis, MSU.

(32) J. Bofill, Ph.D. thesis, MIT.

(33) A. Mukherjee, Ph.D. thesis, MIT.

(34) A. Bertin, et al., Phys. Lett. 42B (1972) 493.

J. V. Beaupre, et al., Phys. Lett. 37B (1971) 432.

(35) S. D. Drell and T. M. Yan, Phys. Rev. Lett. 24 (1970) 181.

G. B. West, Phys. Rev. Lett. 24 (1970) 1206.

(36) S. J. Brodsky and G. R. Farrar, Phys. Rev. Lett. 31 (1973) 1153; Phys. Rev. D11 (1975) 1309.

(37) Comput. Phys. Commun. 10 (1975) 343.

(38) A. Sirlin, and W. J. Marciano, Nucl. Phys. B189 (1981) 442.

J. F. Wheater and C. H. Llewellyn Smith, Nucl. Phys. B208 (1982) 27.

M. Wirbel, Ph.D.Thesis, University of Dormund (1981), and Heidelberg preprint HD–THEP 82–7.

S. Dawson, J. S. Hagelin, and L. Hall, Harvard preprint HUTP–80/A090.

(39) J. I. Friedman, private communication.

L. W. Mo. AND Y. S. Tsai, Rev. Mod. Phys. 41,(1969)205.

A. De Rujula, R., Petronzio, and A. Savoy-Navarro, Nucl. Phys. B154 (1979) 394.

(40) A. Bodek and J. C. Ritchie, Phys. Rev. D23 (1980) 1070; Phys. Rev. D24 (1981) 1400.

(41) H. Abramowicz, et al., Z. Physik C15 (1982) 19.

M. Holder et al., Phys. Lett. 74B (1978) 277.

(42) J. J. Aubert, et al., Phys. Lett. 123B (1983) 275;

A. Bodek, et al., Phys. Rev. Lett. 50 (1983) 1431.

Phys. Rev. Lett. 51 (1983) 534.

R. G. Arnold, et al., Phys. Rev. Lett. 52 (1984) 727.

(43) see e.g., R. L. Jaffe, et al., Phys. Lett. 134B (1984) 449.